Chapter 13 Antenna Measurements

13.1 Antenna Measurement Equipment

Figure 13-1 illustrates the elements of antenna measurement equipment for an outdoor range. Outdoor ranges are built to handle large test antennas and transmit over long distances to reduce quadratic phase error across the aperture. The usual practice is to have the signal transmitted from a source antenna and received by the antenna under test (AUT). Although by reciprocity, the antenna range could be operated with the transmitter connected to the AUT and the receiver to the source antenna and it would produce the same patterns. The source antenna with a narrow beam is placed on a high tower to reduce the signal that bounces off soil from significantly affecting the signal strength and phase across the receiving aperture. Section 13-2 discusses the elevated range signal distribution across the AUT. A positioner on the source tower controls the polarization, but the differing soil reflections (Section 1-18) may necessitate separate calibrations of the horizontal and vertical polarizations. As shown in Figure 13-1, the AUT is mounted on a heavy azimuth over elevation positioner with boresight of the AUT orthogonal to the azimuth axis. The positioning of the AUT can be described as rotations about axes in space as the product of rotation matrices (Section 3-13). If we designate the *z*-axis as the AUT boresight direction between the source and the test positioner, the *x*-axis as the normal to the page of Figure 13-1, and the *y*-axis as vertical, then the positioner operating is explained as first a rotation about the *x*-axis (elevation) followed by a rotation about the new *y*-axis (azimuth) with *z*-axis rotation as AUT polarization.

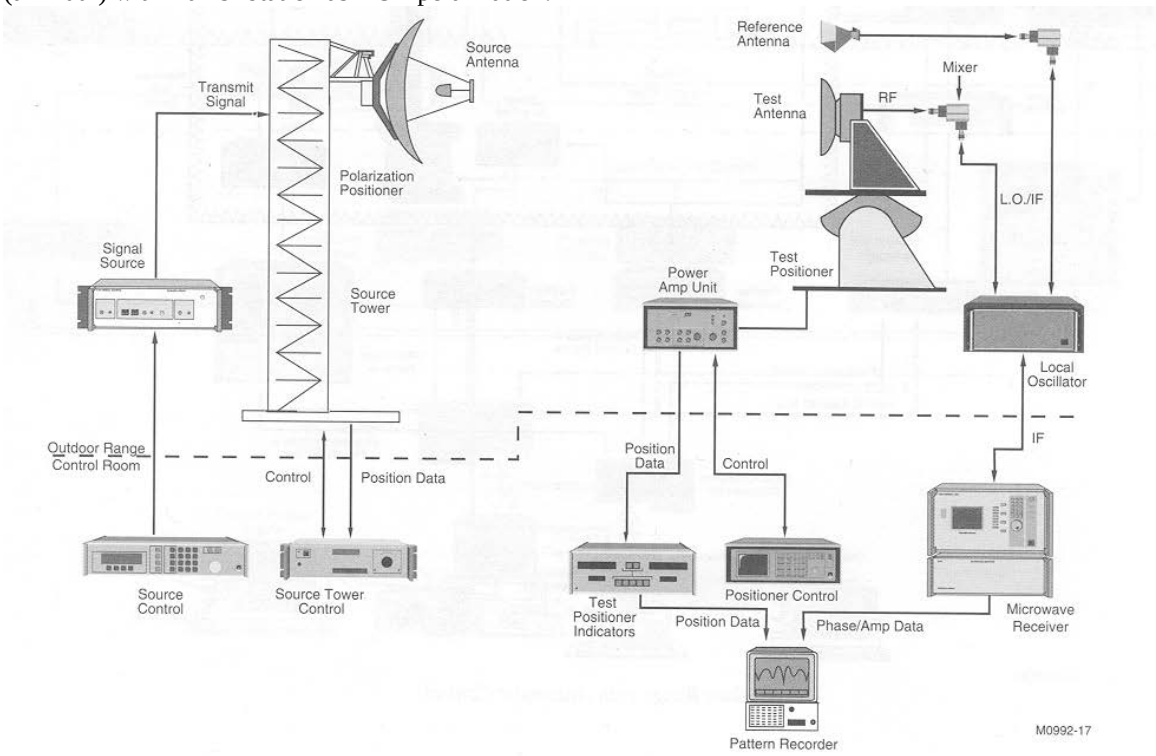

Figure 13.1 Outdoor antenna range equipment

Figure 13-2 shows the heavy positioners: azmiuth-over-elevation and elevation-over-azimuth. The elevation-over-azimuth position can be analyzed as two rotations. The elevation axis rides on top of the azimuth table and changes direction as azimuth moves. Again, if we mount the *z*-axis of the antenna orthogonal to azimuth axis so it points parallel to the ground, the lower rotation is about the *y*-axis that rotates the *x*-axis of the elevation axis. The second upper rotation is about the new *x*-axis. We calculate the pointing directions by using rotation matrices (Section 3-13).

Each axis of the positioner has either a synchro package or optical encoder to report on the angle. The positioner controller uses this information to set its angle. A synchro is a rotating transformer. The usual three-phase synchro is

made with three windings in the stator with their axes separated by 120º. The rotator contains a single winding. When current flows through the rotator (400 Hz), it induces voltages in the three windings proportional to the angle of the rotator winding with respect to the stator winding axes. In a manual system these three voltages are applied to the three stator windings of a follower synchro whose rotator is not driven but connected to the dial of a rotating pointer and rotates to the same angular position. The single synchro gives limited resolution. A polar plotter uses another follower synchro to drive its table while the radial arm is driven by the receiver output. To improve resolution a second synchro is added to the package and connected to the shaft by 36:1 gearing to produce a complete synchro rotation for every 10º. Rotating indicators are built to follow both synchro outputs. It appears that the two dials have been geared in the same 36:1 ratio but they are just independent dials. Both the angle indicators and the polar plotting tables contain friction clutches to allow manual setting of zero. Manual rectangular plotter also uses the synchro voltages to drive a follower synchro whose rotation drives the shaft that moves the paper linearly through properly sized gearing.

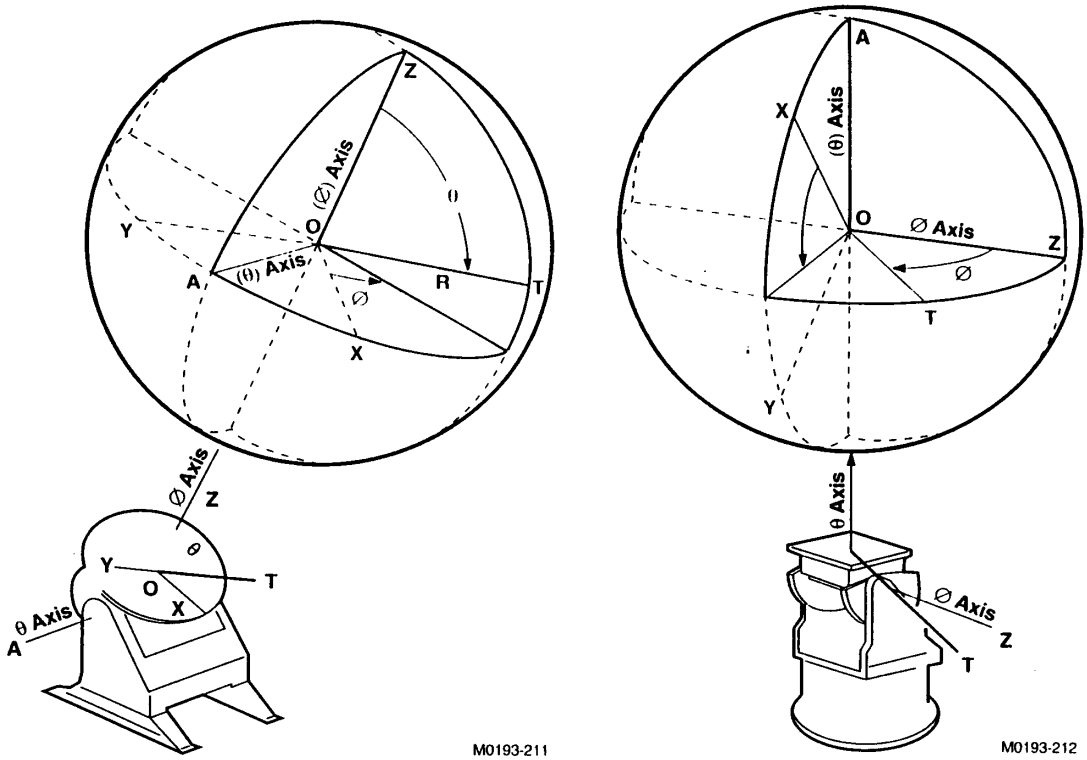

Figure 13-2 Heavy positioners: (*a*) azimuth-over-elevation, (*b*) elevation-over-azimuth

Manual pattern plotting can only operate on one frequency at a time. The receiver and synthesized transmitter can be phased locked to differ in frequency by the IF to allow measurement of multiple frequencies while as the positioner axis is rotating. This produces a more interesting control problem. First, sampling of the two synchro outputs produces a digitized output that can be fed into a controller. We can either measure the multiple frequencies while the positioner is moving or stop the positioner at each measurement angle and step through the frequency list. The second step mode produces more accurate positioning, but increases the run-time as the positioner must overcome inertia after each step. To prevent overshoot of the step angle, the positioner controller should slow the rate of rotation as the stop angle is approached. Adding a tachometer to the axis adds another state variable to the control system and reduces overshoot that can cause the angular cycling around the commanded angle. In the continuous measurement mode of operating the angle where measurement happens at each frequency is spread over a range of angles. Ideally, for a given frequency each measurement will be at the same offset from the triggering angle for the first frequency. Tachometer feedback improves the controller's ability to maintain a constant rotation rate because the rotating axis may have binding in the shaft or unbalancing the antenna from the axis may cause uneven rotating rates. The digitized output of the angular position is stored along with measurement of each frequency and the fluctuations of angle can be corrected, if necessary. Digitizing the output of a single synchro produces a resolution of 0.01º, a dual synchro a resolution of 0.001º, and an optical encoder a resolution of 0.0001º. Figure 13-1 contains a

power unit to provide the power necessary to drive the positioner motors while the controller operates independent of motor size.

The receiver uses two channels to allow measurement of phase as well as amplitude. We add the second channel to phase lock the receiver to a fixed level signal that has traveled an independent path. Figure 13-1 shows a reference channel horn placed off to the side of the rotating antenna that both phase-locks the receiver and provides the channel for a relative phase measurement. This reference channel samples the incident wave front. The synthesized transmitter generator returns to same frequency within the resolution of the digital phase-locked loop, but not the same phase. The difference between the two channel paths determines the phase difference measured. If the cables that carry the signal or local oscillator are not stable, phase will drift with time and cause measurement error. For this reason we mount the mixer and local oscillator generator close to the receiving antennas and carry the IF over the longer cables. As receiver and synthesizer technology improves, the number of frequencies that can be measured increases. We either become overwhelmed with data or we can use signal processing by converting to the time-domain to remove unwanted range reflections in a software gate through windowing the time response. Of course, all these measurements must be stored in computer memory while the computer provides executive control of the transmitter, receiver, and positioner controller.

13-2 Elevated Outdoor Range

Reflection of the signal from the soil in an outdoor range produces measurement error. When we raise the source antenna and AUT, we reduce these errors. Figure 13-3 illustrates the geometry of the elevated range.

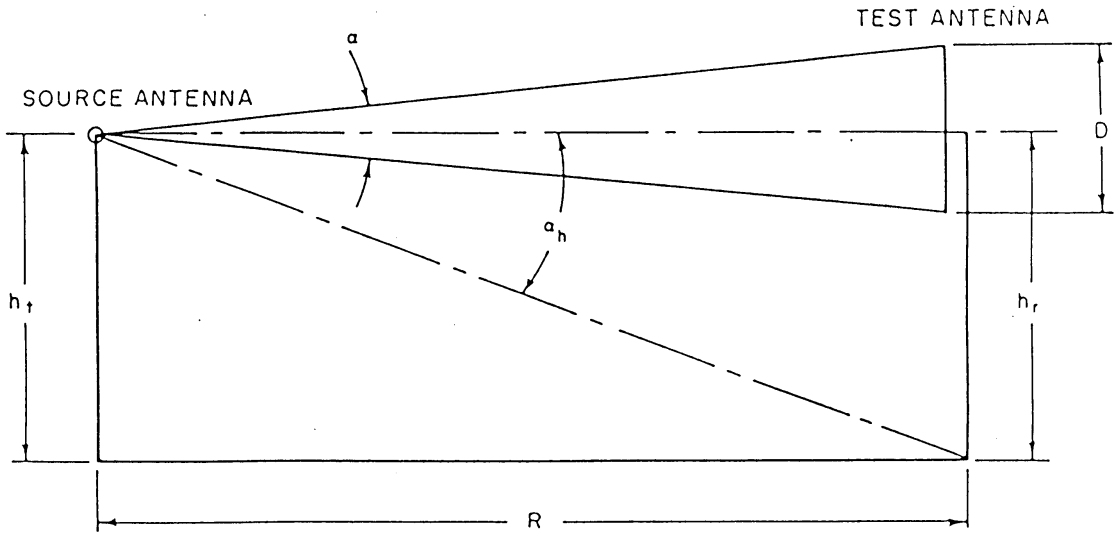

Figure 13-3 Elevated outdoor antenna range

The recommended parameters of the elevated range are: $R = 2D^2/\lambda$, source height h_t = receive height h_r, receive height $h_r = 4D$. The minimum range distance corresponds to the quadratic phase factor $s = 0.062$, which generates about 0.1 dB loss for a uniform distribution (Tables 4-42 or 4-43) with a smaller effect for tapered distributions. Figure 4-33 illustrates that this quadratic phase error across the aperture reduces the first null depth and raises the measured first sidelobe of distributions for low sidelobes. The second pattern sidelobe and null show little error. We need to be concerned about the pattern level of the source antenna directed toward the reflection region. Figure 13-4 shows the amplitude ripple in the aperture plane of a 60-foot antenna elevated range when measuring at 1.9-GHz using a 90º beamwidth source antenna (for example,a microstrip patch or dipole over a finite ground plane). The difference between reflection of horizontal and vertical polarizations [Figure 1-9] from soil produces significantly different responses. The horizontal polarization has amplitude ripple of at least 10 dB, which corresponds to an interfering signal 5.6 dB below the direct path signal [Scale 1-8]. The reflection from soil is less for vertical polarization and the 3.4 dB ripple corresponds to an interfering signal 14 dB below the direct. The amplitude ripple means there is an associated phase ripple as well. Vertical polarization has a maximum phase error of 11º [Scale 1-9] while horizontal polarization phase error is 27.7º. These errors are unacceptable. Figure 13-4 illustrates that the

phase of the vertical and horizontal reflections are 180º out of phase because the peaks and nulls are offset for the two polarizations.

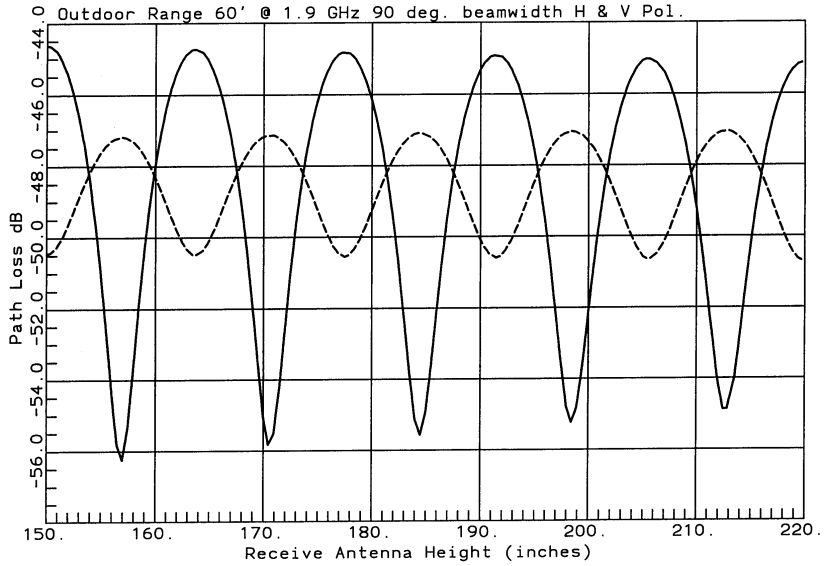

Figure 13-4 Aperture plane fields using a 90º beamwidth source on 60-foot elevated range with source at 15-foot height (*a*) solid – horizontal polarization, (*b*) dashed – vertical polarization

Using a higher gain source antenna reduces the ground reflection of the elevated range and reduces aperture ripple. Figure 13-5 shows how replacing the low gain source antenna with a standard gain horn with 17 dB gain reduces the interfering signal. The interfering signal is 17 dB to 23 dB below the direct for horizontal polarization and about -25 dB for vertical polarization. These errors may be acceptable for some applications.

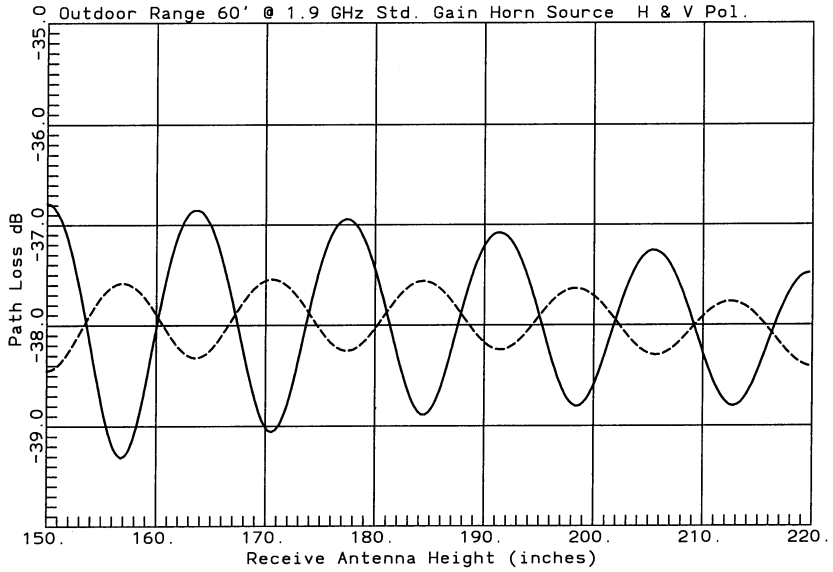

Figure 13-5 60-foot elevated antenna range over soil at 1.9-GHz using a standard gain antenna as source (*a*) solid – horizontal polarization, (*b*) dashed – vertical polarization

An aperture antenna integrates the aperture ripple and produces a lower ripple when an aperture antenna samples the aperture. Figure 13-6 plots the aperture field for a 6-foot diameter reflector measured on a 600-foot antenna range at 4 GHz. The plot shows nearly equal ripple for horizontal and vertical polarization because the reflection approaches grazing angles less than the Brewster angle where both polarizations have the same phase and similar amplitude. The nearly 2-dB ripple means the interfering signal is quite significant (-19 dB). Figure 13-7 illustrates amplitude

ripple along the distance axis. Instead of reducing monotonically, the down range pattern ripples. Both the vertical and down range ripple rates are larger than a wavelength.

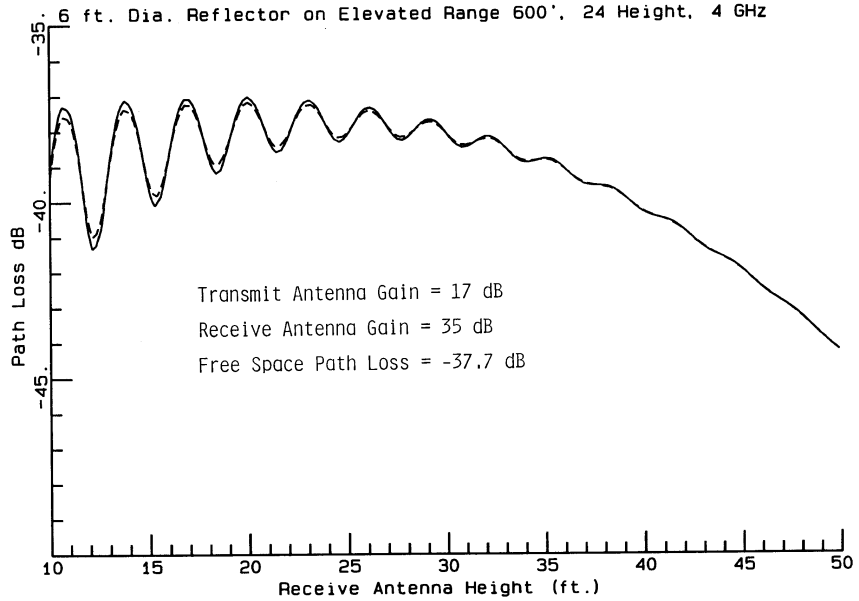

Figure 13-6 Aperture field in the vertical plane of an elevated range at 4 GHz for range 600 feet and a height of 24 feet. (*a*) solid – horizontal polarization, (*b*) dashed – vertical polarization

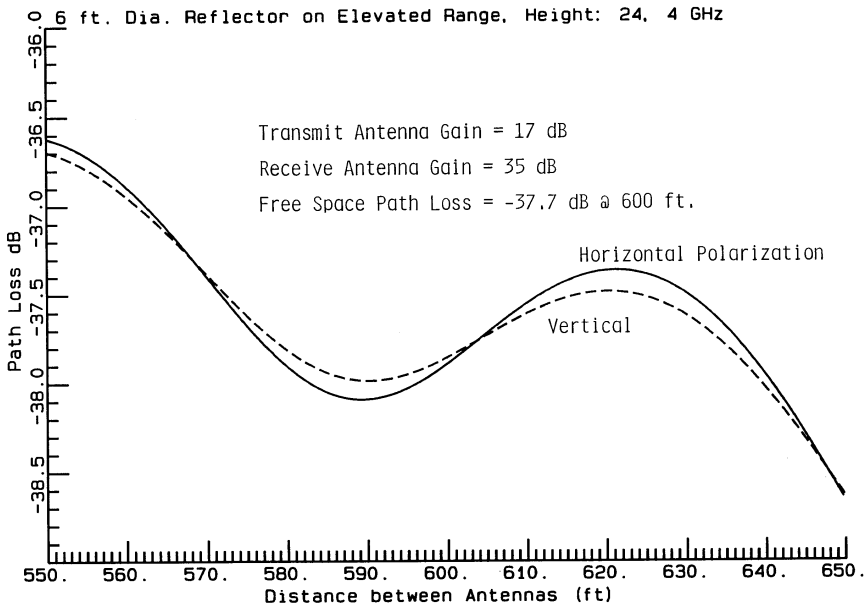

Figure 13-7 Down-range ripple on elevated antenna range at 4 GHz and 24-foot height

We can elevate the range further than the 4*D* suggested antenna height to reduce ground reflection. Figure 13-8 gives the aperture plane when the transmitting and receiving antennas are raised to 40 feet. This height produces a smooth wide maximum at a 40-foot height. The figures of this section show it is important to access aperture ripple in an outdoor elevated range before blindly measuring on one of these facilities.

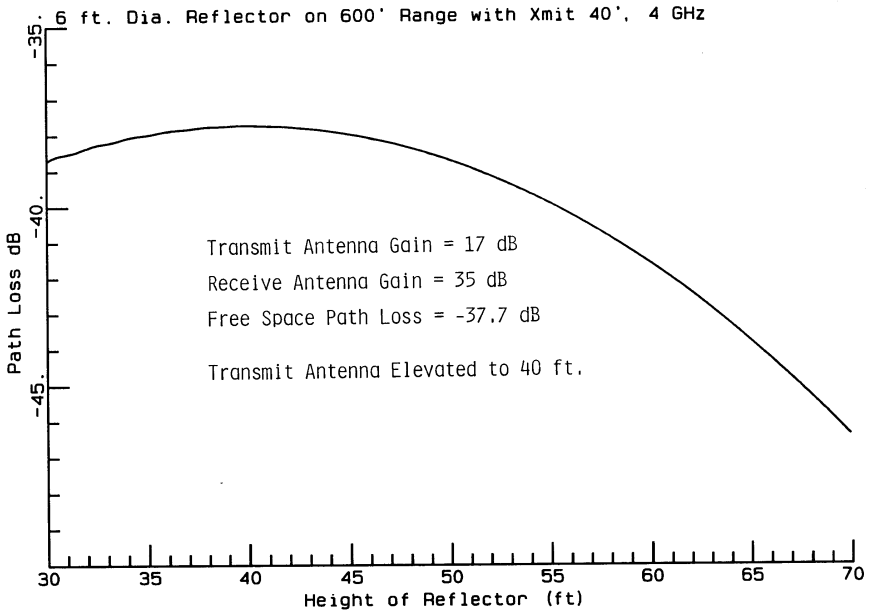

Figure 13-8 Aperture distribution integrated by 6-foot aperture on a 600-foot range with source and receiving antennas elevated 40 feet at 4 GHz.

We can reduce the effect of the soil reflection by adding diffraction fences to the range to redirect the reflections away from the AUT. Figure 13-9 shows the plan view of an outdoor range with a series of five diffraction fences.

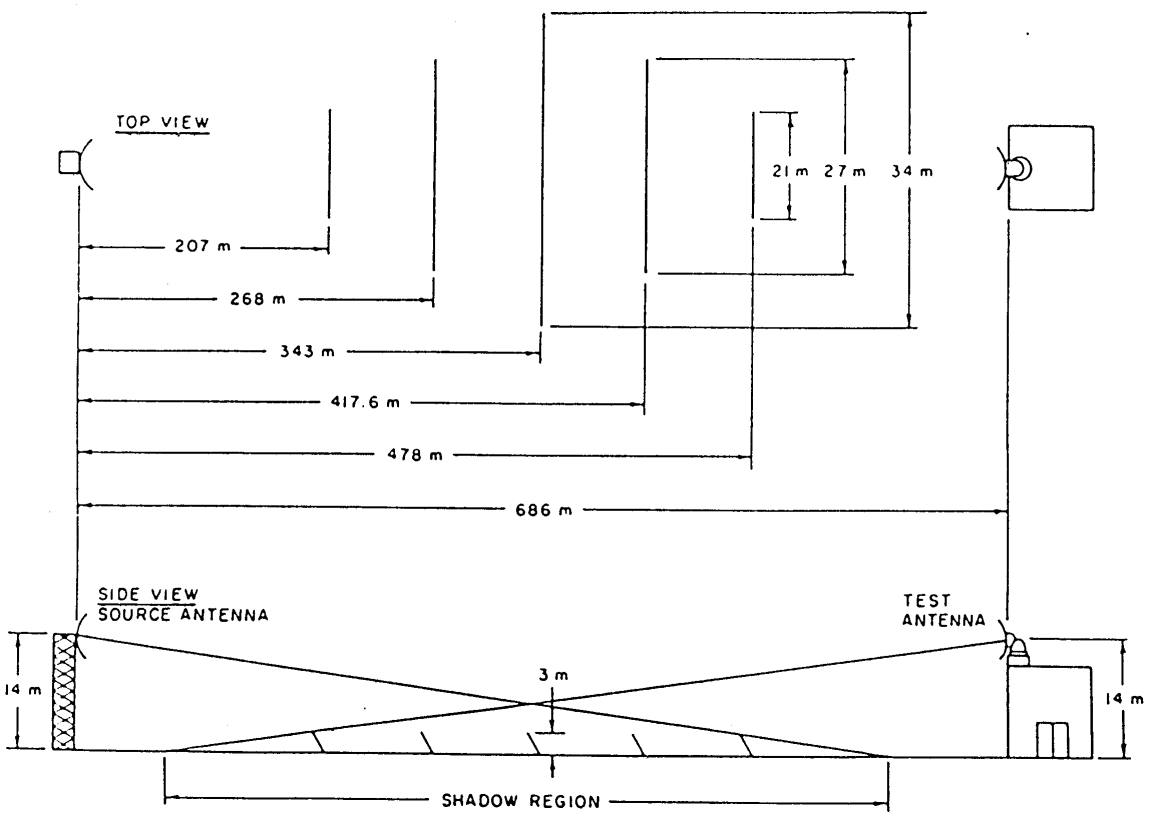

Figure 13-9 Diffraction fences on elevated range

We can reduce the knife-edge diffraction from the top of the fences by serrating them as shown in Figure 13-10. To fully assess the effectiveness of the fences it would be best to probe the aperture fields.

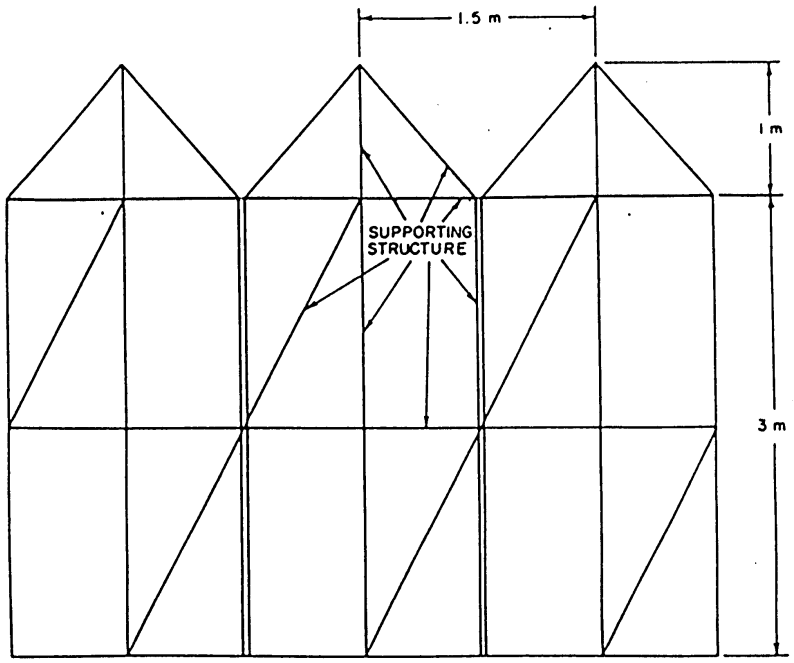

Figure 13-10 Serrated top diffraction fence

13-3 Ground Reflection Outdoor Range

The ground reflection range uses the soil reflection to smooth the aperture distribution at the AUT by phasing it to add with the direct signal. We lower the source antenna to height determined by the range length, wavelength, and AUT antenna height. The source antenna height is approximately $\lambda R/(4h_r)$. For a relative smooth flat ground plane, we located the receive antenna height $h_r > 3.3D$ for 0.25 dB vertical ripple. Figure 13-11 gives the elevation view of the range.

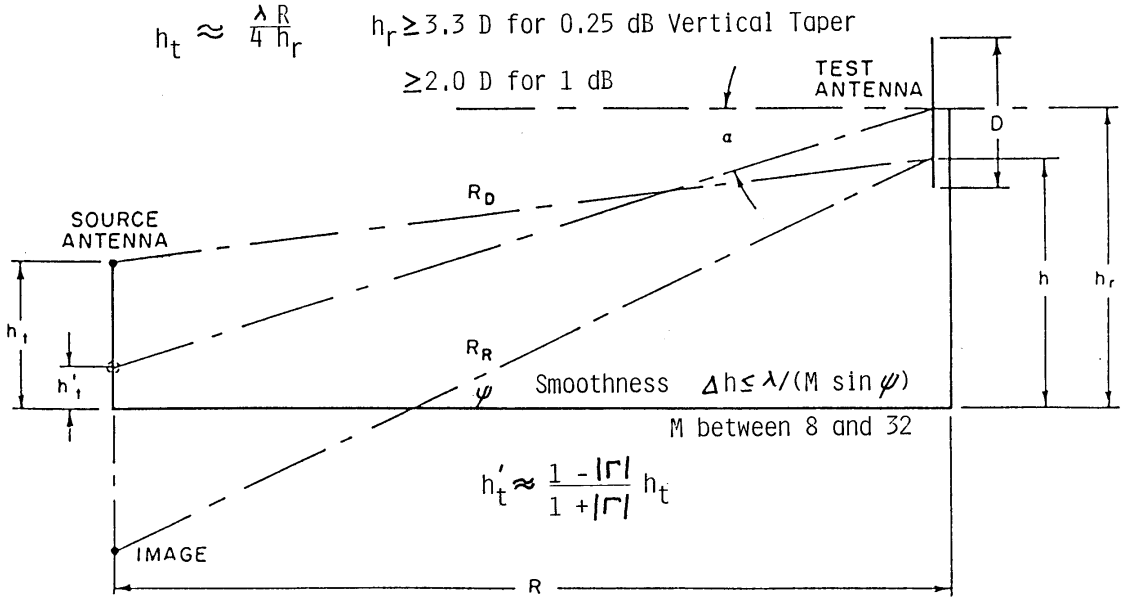

Figure 13-11 Ground reflection outdoor range.

Figure 13-12 plots the vertical probe pattern of a 600-foot ground plane range operating at 4 GHz and shows the smooth distribution instead of the rapid ripple of the elevated range. The 0.25-dB ripple ranges from 16- to 25-ft for

horizontal polarization and from 15- to 24-ft for vertical polarization. The flat-top of the two curves differ by 1-ft and average at 20-ft. The second thing to notice about this plot is the difference between the horizontal and vertical polarizations. Separate calibrations using a gain standard are necessary for the two polarizations to remove this difference from the measurements. At 5-GHz, the proper source height reduces to 1.44-ft. Figure 13-13 gives the frequency response of the range for a fixed source height and shows the variation in the vertical probe amplitude for 3-, 4-, and 5-GHz. This figure illustrates the necessity of varying the source height after changing frequency. A tapered anechoic chamber is modeled after the ground reflection range and its response is sensitive also to the distance of the source from the walls in the narrow tapered source end.

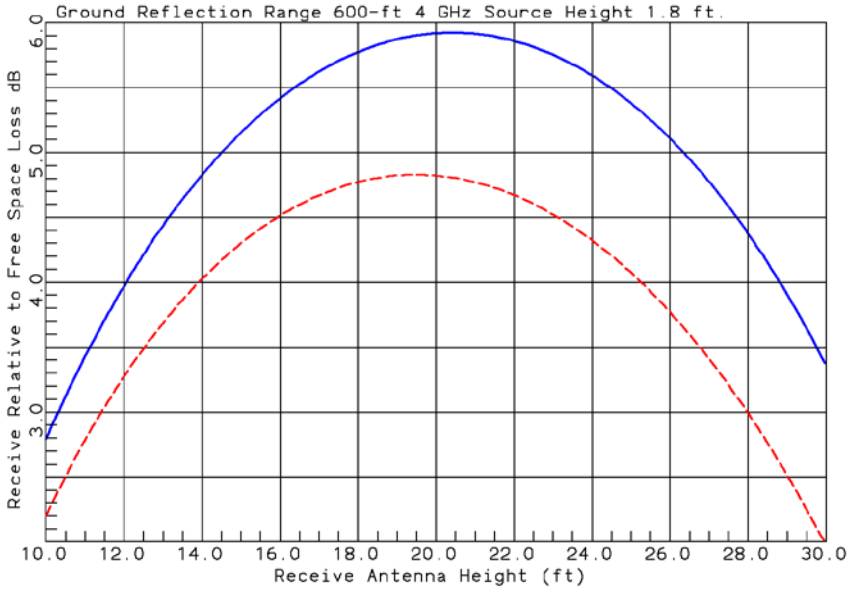

Figure 13-12 Vertical probe on 600-ft ground reflection range @ 4 GHz with 1.8-ft source height (*a*) Solid – Horizontal Polarization, (*b*) Dashed – Vertical Polarization

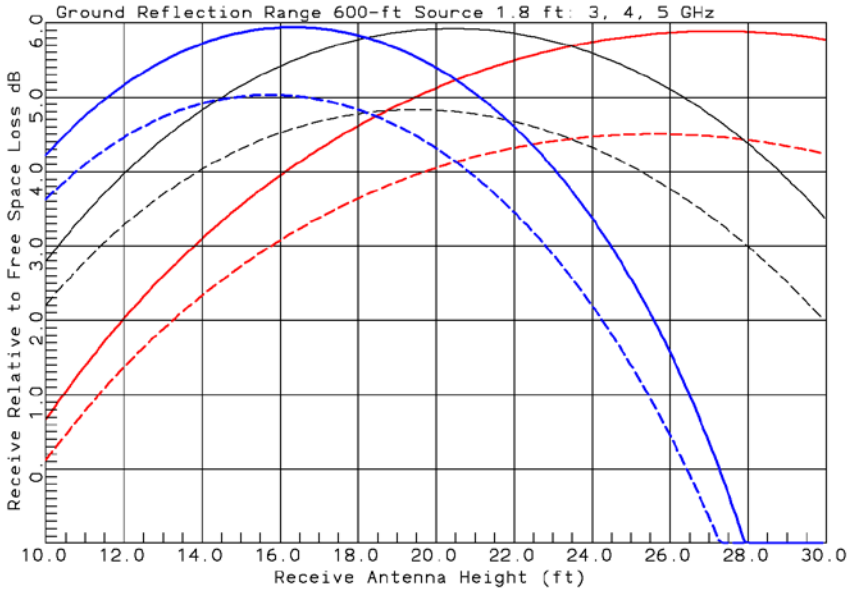

Figure 13-13 Vertical probe on 600-ft ground reflection range with 1.8-ft source height: 3-GHz – red, 4-GHz – black, 5-GHz – blue. (*a*) Solid – Horizontal Polarization, (*b*) Dashed – Vertical Polarization

13-4 Indoor Antenna Ranges (Anechoic Chambers)

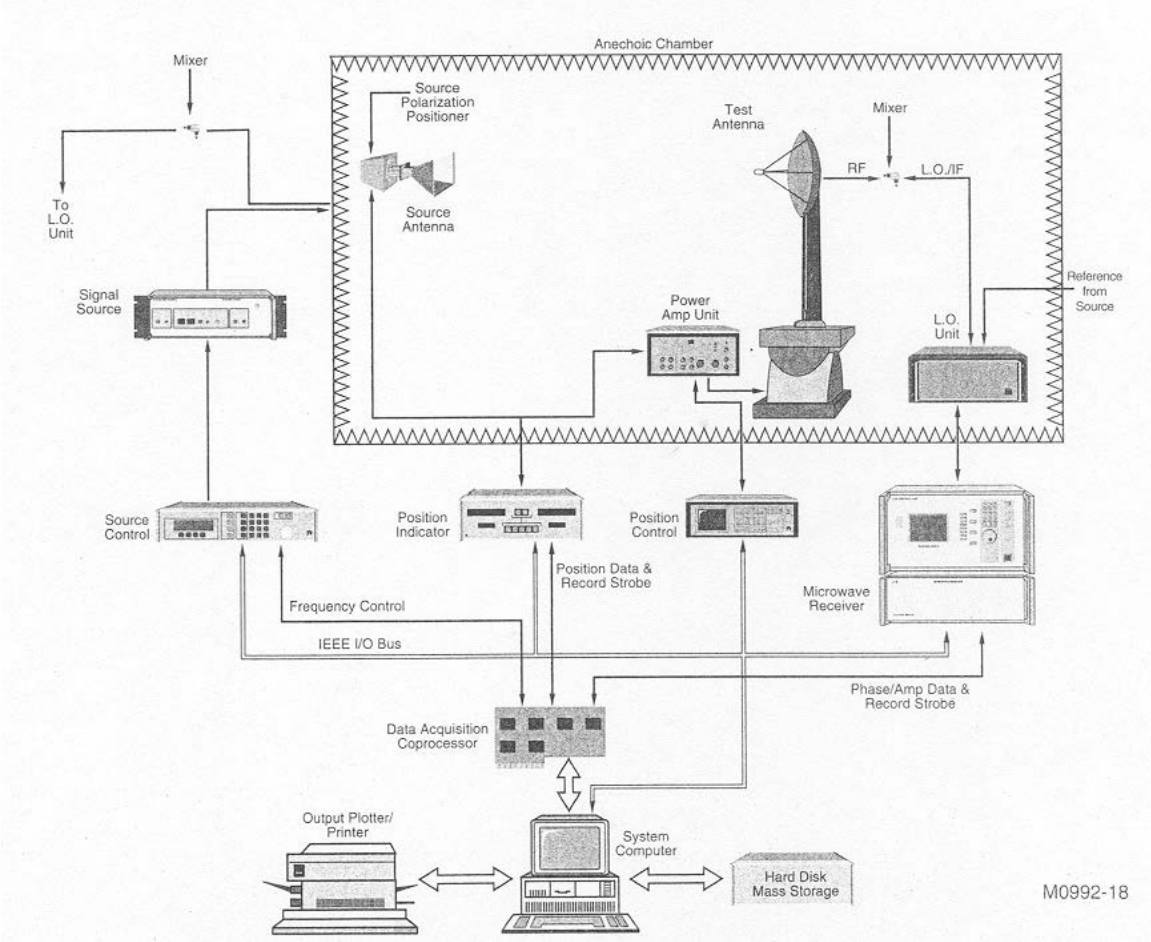

Figure 13-14 Instrumentation of indoor antenna range.

Figure 13-14 illustrates the arrangement of equipment used in an indoor antenna range. The anechoic chamber is lined with absorber to prevent wall reflections from reaching a quiet zone centered on the receiving antenna located at one end. We use thick absorber where a wave can reflect into the quiet zone with a single bounce and thinner absorber where it takes multiple bounces. Chambers are designed using ray tracing and knowledge of the reflection characteristics of the absorber. The chamber size and absorber thickness determine the lowest operating frequency, whereas the fineness of the absorber points determines the highest operating frequency. The absorber is carbon-loaded polyurethane foam treated with fire-retardant chemicals, which can be leached out by water (ceiling leaks). The absorber should be self-extinguishing when the source of flames is removed. The source antenna is centered vertically along the chamber axis (not as shown) on positioner that rotates the polarization of the antenna. The usual positioner in a chamber is a model tower, which moves the antenna directly in the spherical coordinate system and allows axial movement to center the antenna over the azimuth axis when mounted on the rotating head. The RF equipment uses a synthesized transmitter and a tracking receiver to allow measurement of multiple frequencies in the same manner as outdoor ranges. Figure 13-14 connects the reference channel mixer directly to a coupled signal from the transmitter.

A rectangular chamber is similar to an elevated outdoor range where the source and receiving antenna are located the same distance from the walls. The rectangular chamber uses thick absorber on the sidewalls and back-wall for single bounce reflections. The tapered chamber purposely uses wall reflections near the source to smooth the field in the quiet zone in the same manner as the ground reflection range. Figure 13-15 gives the field ripples in the quiet zone of the two chambers. The tapered chamber uses thin absorber in the chamber throat to allow reflections at low

frequencies, whereas the back-wall has full-sized absorber to prevent reflections at the lowest frequency of operation.

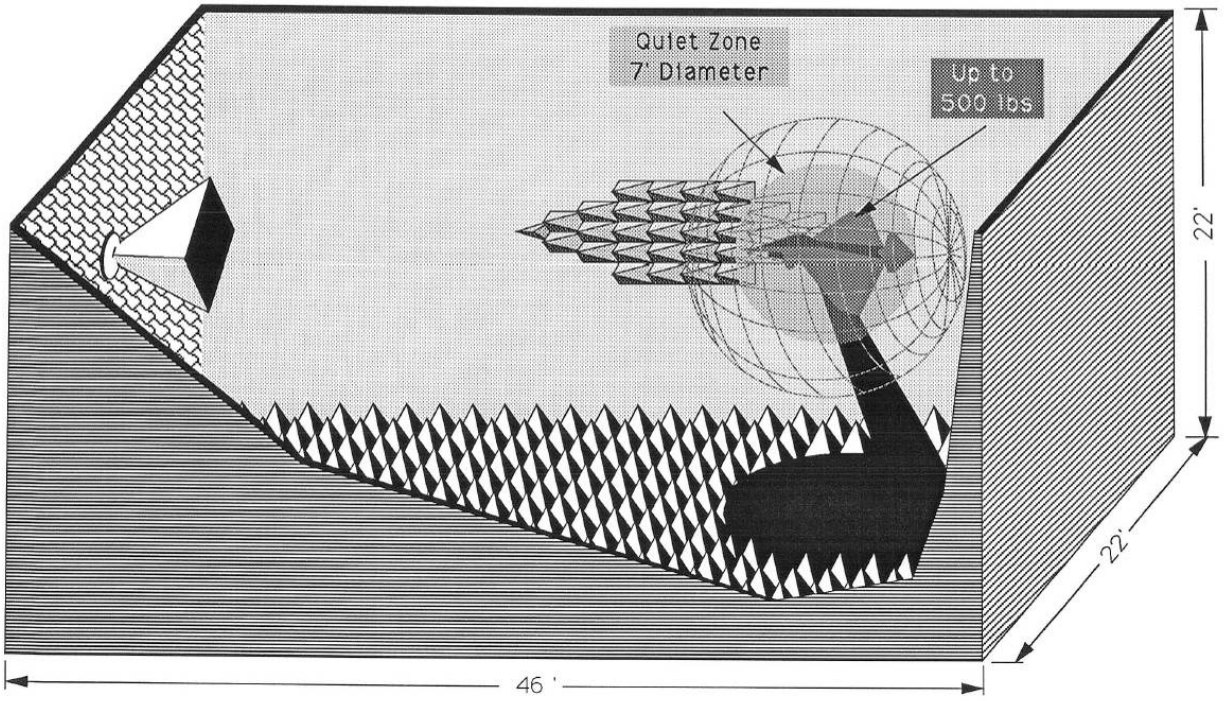

Figure 13-15a Rectangular Chamber with RCS Target

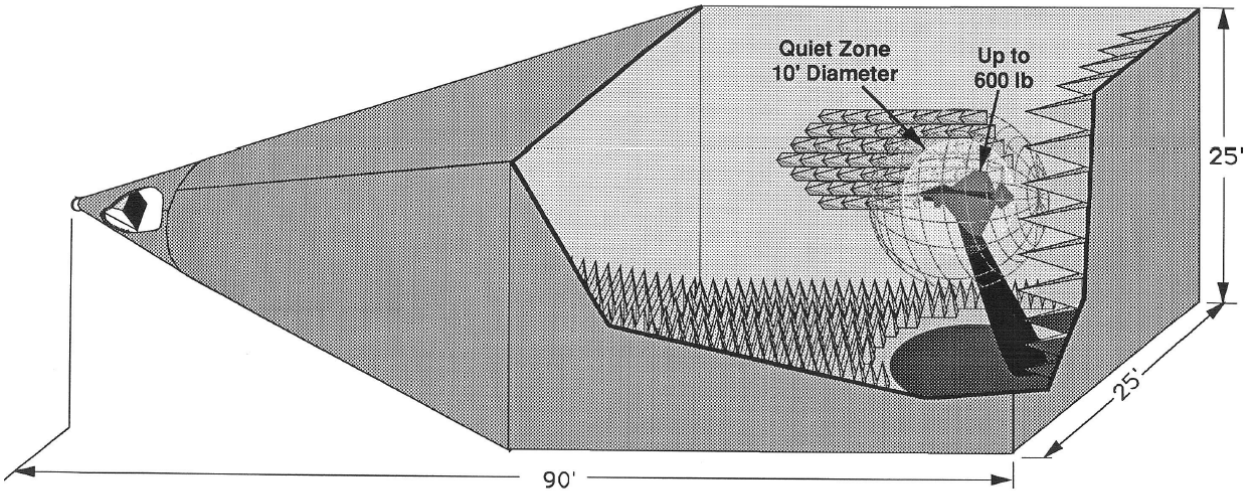

Figure 13-15b Tapered Chamber

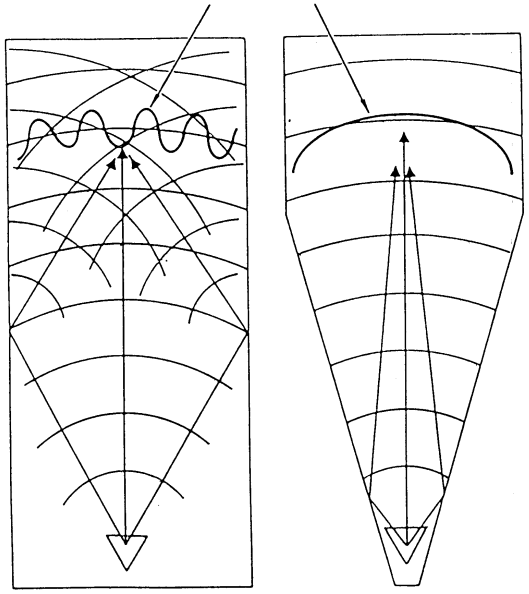

Figure 13-15c Reflections and quiet-zone field variations in (*a*) rectangular and (*b*) tapered chambers

Because the tapered chamber is a ground reflection range that relies on wall reflections, its quiet-zone fields are sensitive to the source location and beamwidth. A series of experiments need to be performed to find the proper location for the source antenna for each frequency band. To properly illuminate the walls, the source antenna directivity should be no more than 15 dB. We probe the fields in the quiet zone to determine its ripple. Figure 13-16 shows the effect of source location using a geometric optics ray analysis of a tapered chamber.

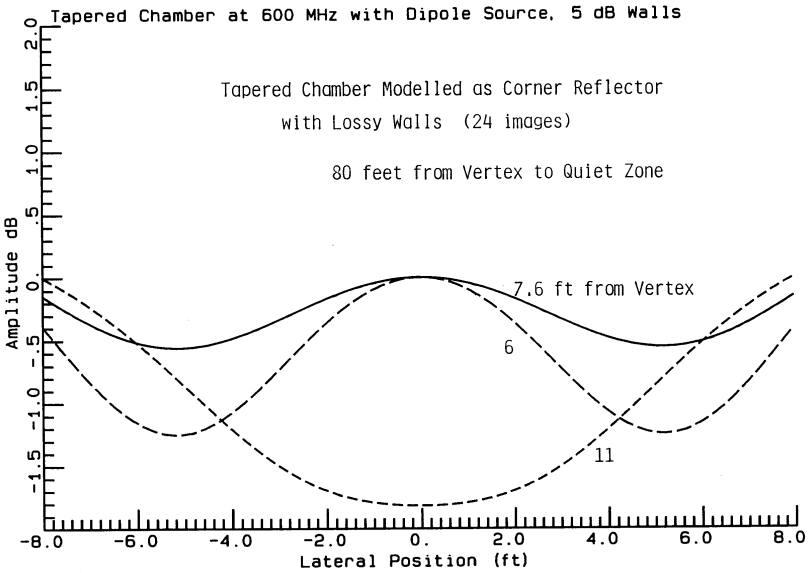

Figure 13-16 Tapered chamber model quiet-zone fields with various source locations measured from the chamber vertex

Figure 13-17 shows a field probe where a receiving antenna (a log periodic dipole antenna as pictured) is moved along a horizontal track to measure the quiet-zone ripple. Of course, the field probe will cause some chamber reflections as the track interacts with the receiving antenna. Another type of field probe places the probe antenna on a vertical dielectric rod and the moving track is placed on the floor of the chamber to reduce chamber reflections due to the probe itself. Each probe contains a synchro package to report on its location and allow plotting or digital recording versus position.

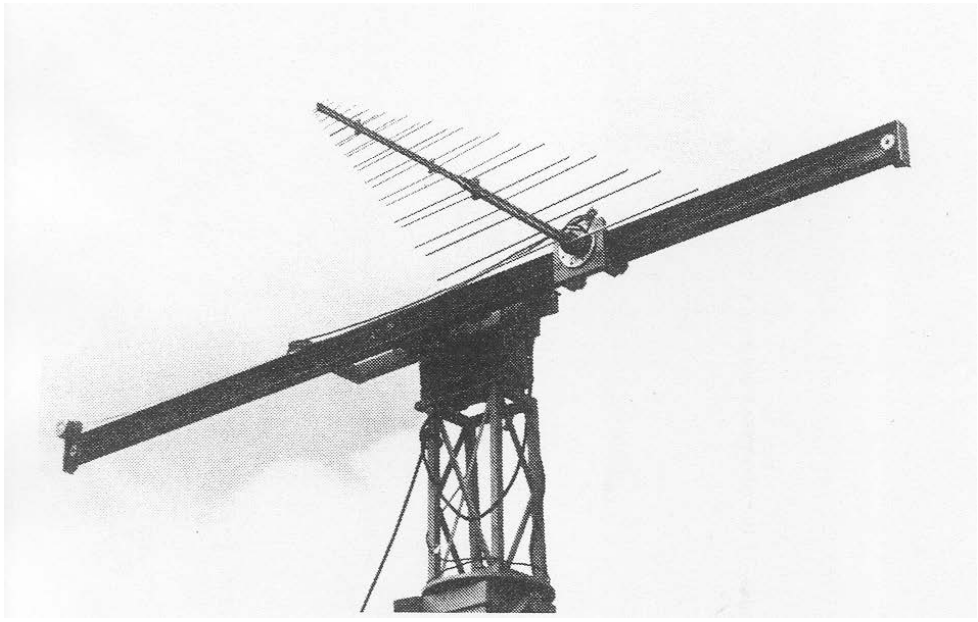

Figure 13-16 Field probe

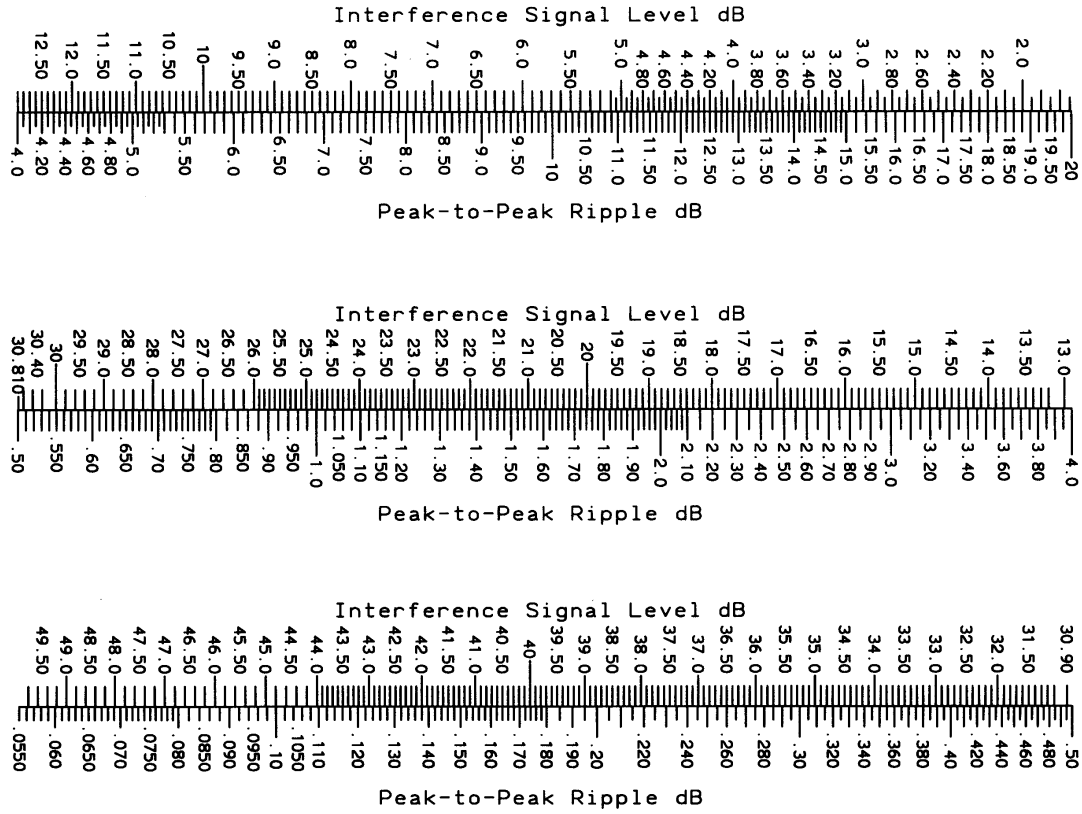

Scale 13-1 Amplitude ripple due to multipath

Chambers are specified to have limited reflections into the quiet-zone because these cause measurement errors from multipath. A usual specification is -40 dB or less. Scale 13-1 is an expanded Scale 1-8, whereas Scale 13-2 is an expanded Scale 1-9. Figure 13-17 illustrates the geometry of the free-space VSWR measurement of a chamber. The

moving probe allows the recording of the standing wave in the chamber due to addition of the multipath signal to the direct signal. Rotating the probe antenna reduces the direct signal relative to the wall reflection and increases the ripple by the probe pattern to allow measurement.

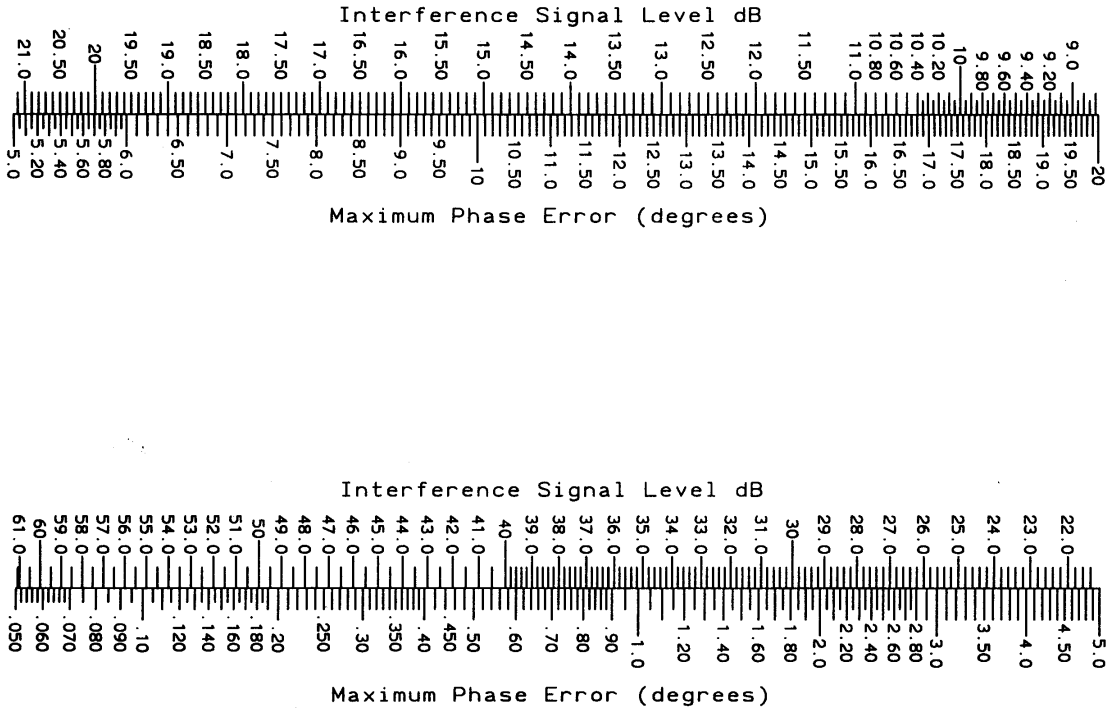

Scale 13-2 Peak phase error due to multipath

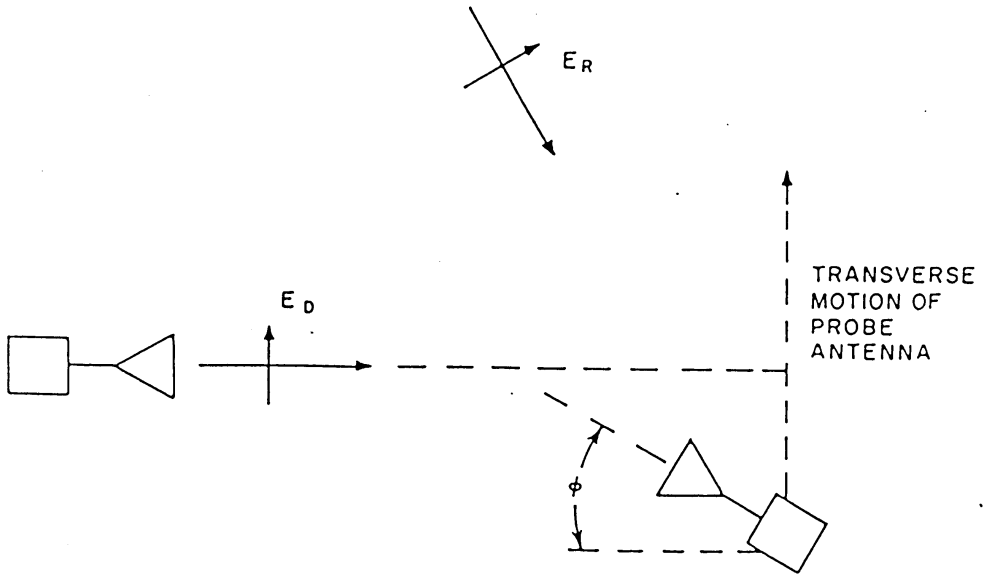

Figure 13-17 Free-space VSWR measurement of chamber reflections

13-4.1 Additional Loss when Measuring Aperture in the Near-field

Assume an antenna under test (AUT) is far enough from the chamber walls that the wall reflections can be ignored. Define a near-field scaling factor, k, so the measurement distance = 2*D**2*k/wavelength. The approximate quadratic phase factor of the measurement is S = 1/(16*k). Compute the aperture diameter or width in wavelengths: DW=D/wavelength, the equivalent k factor used below can be increased by the factor: Sqrt(1 + (1/(4*k*DW))**2) for more accurate results, but for most apertures this factor is nearly one.

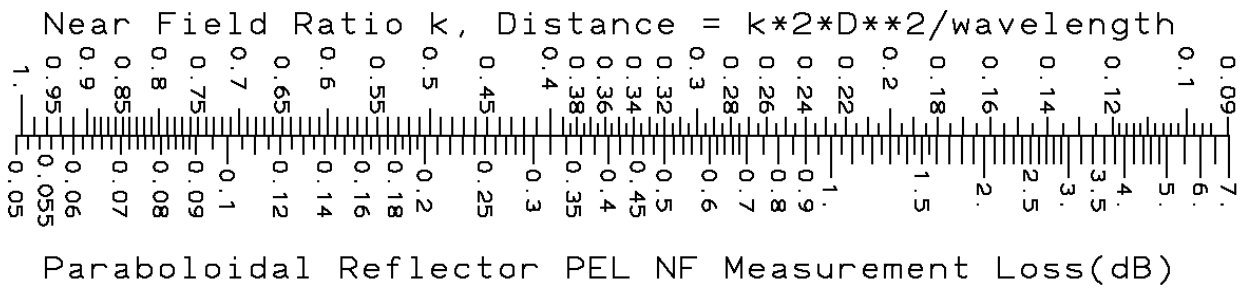

Scale 13-3 Quadratic Phase Error for Paraboloidal Reflector Measured in Near-field

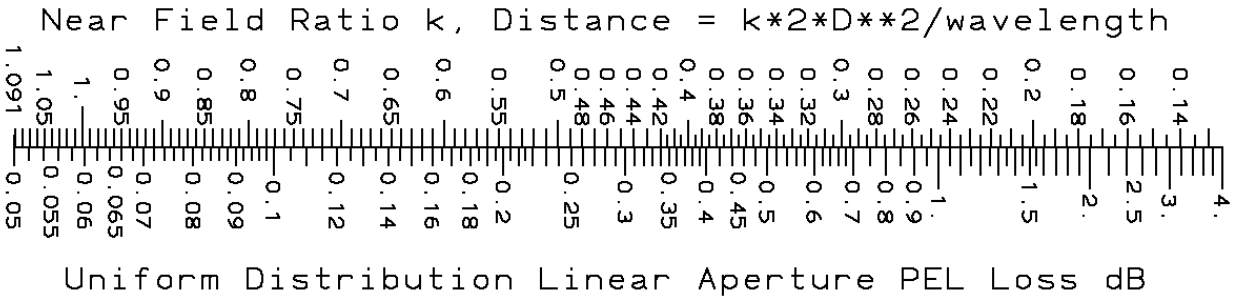

Scale 13-4 Quadratic Phase Error Loss of Uniform Linear Distribution

Much smaller k than given on the scale soon produce a pattern dip on axis and should not be used with a uniform distribution.

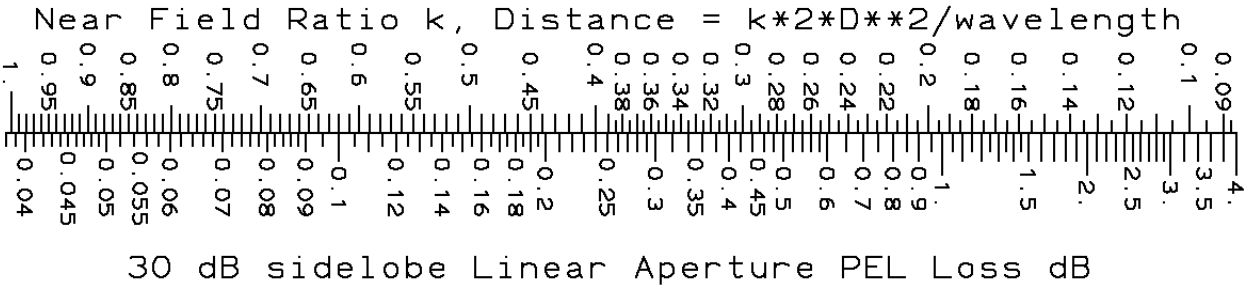

Scale 13-5 Quadratic Phase Error Loss of 30 dB Sidelobe Linear Distribution

A rectangular aperture antenna with near field ratios k(e) and k(h) in the principal planes would have a total measurement loss given by the sum of the values for each plane given by the scales above.

Additional loss occurs due to the extra taper loss across the aperture, but it is small and can be ignored in most cases. The pattern of the chamber feed horn increases the amplitude taper across the antenna depending on its beamwidth. The pattern angle of the feed is related to the near field ratio k and the aperture width in wavelengths DW
Feed Angle = acos(1/sqrt(1+ 1/(2*k*DW)**2)
There is additional taper loss due to the path distance to the edge relative to the aperture center:
taper (dB) = 10*Log(1+1/(2*k*DW)**2)

We sum the tapers due to the feed pattern and path length ratio and consider the amplitude taper losses to the AUT. For a paraboloidal reflector the taper loss is given by the scale.

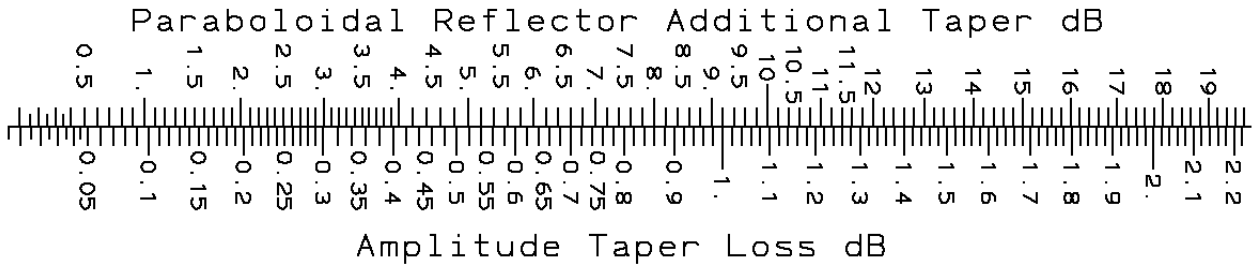

Scale 13-6 Additional Amplitude Taper Loss of Paraboloidal Reflector

A linear antenna's taper can be approximated by a cosine squared on a pedestal distribution where the 30 dB sidelobe antenna has a 13 dB taper. Use the scale below and subtract the loss for a 13 dB taper from the total loss now across the antenna due to the taper for a low sidelobe antenna while a nearly uniform distribution uses the scale without adjustment. Of course, the near-field measurement eliminates pattern nulls and raises sidelobe levels.

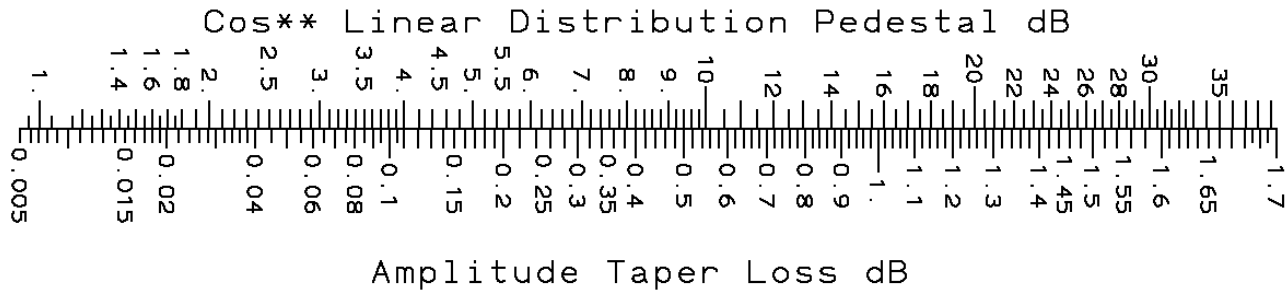

Scale 13-7 Additional Amplitude Taper Loss of Linear Cosine^2 + Pedestal Distribution

13-5 Model tower positioner and phase center measurement

The model tower positioner has a horizontal track at its base that allows movement of a horizontally-mounted rotating head positioner that is mounted on a long dielectric tube to place the head in the center of the chamber vertically. The drive motor, synchro package and possibly a tachometer are located in the base with a dielectric drive-shaft located in the center of the dielectric support tube of the positioner. The dielectric tube reduces reflections at low frequencies, but at higher frequencies it is necessary to wrap the support in absorber when the dielectric tube becomes a significant scattering object. Rotation of upper axis moves the antenna about the Φ coordinate of spherical coordinates. When we mount the model tower on an azimuth table, its rotation moves the antenna pointing by the θ spherical coordinate.

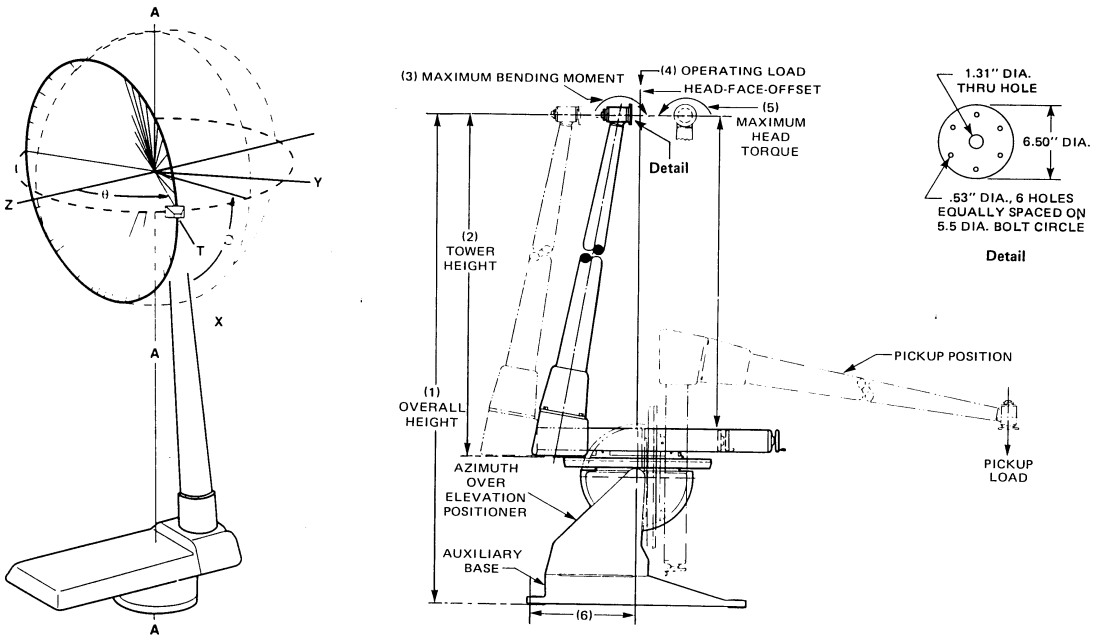

Figure 13-18 Model tower positioner (a) on azimuth positioner, (*b*) on azimuth-over-elevation

13-5.1 Phase center measurement

The model tower positioner allows the measurement of antenna phase center because its position can be moved until it rotates about the vertical azimuth axis where phase change is minimum. We need to position the phase center at the focus of a paraboloidal reflector to minimize phase error loss. We use [(Eq. 8-7)], the phase error loss of a paraboloidal reflector, as our measure of phase center where we move the antenna until this integral is a minimum. Given an antenna measurement table, we adjust the phase by applying [(Eq. 3-1)] for movement to a new position $\boldsymbol{r} = (x, y, z)$ using the wave number $\boldsymbol{k} = 2\pi/\lambda(\sin\theta\cos\varphi, \sin\theta\sin\varphi, \cos\theta)$ with all measurements multiplied by $e^{j\boldsymbol{k}\cdot\boldsymbol{r}}$. We rotate the polarization head of the positioner to zero and 90º to obtain the phase center location in the *x* and *y* planes (and axes).

Figure 13-19 shows an antenna mounted on the polarization head axis of a model tower positioner. Although phase center is a general term for the location of the point of minimum phase movement over a range of angles, we divide this into a *z*-axis term called *phase center*, and the location off-axis called *lateral offset.* The feed to produce a beam peak on boresight of a reflector will have a significant pattern level on boresight ($\theta = 0$). We need to apply different techniques than given here for patterns with nulls on boresight such as mode 2 spirals. We measure the pattern phase at equal off-boresight angles relative to the phase at boresight, Ph_1 at θ and Ph_2 at $-\theta$ and compute the phase center and lateral offset.

$$\text{Phase Center } = \frac{(Ph_1 + Ph_2)\lambda}{720(1-\cos\theta)} \tag{13-1}$$

$$\text{Lateral Offset } = \frac{(Ph_1 - Ph_2)\lambda}{720\sin\theta} \tag{13-2}$$

Equations (13-1) and (13-2) use phases in degrees. These assume the measurements were taken by manual control of the positioner with the phases read from a meter and inserted in the equations. Proper measurements do not use negative values of θ but are limited to the range 0º to 180º, but these equations assume negative values were used. For a linearly polarized antenna such as a horn or dipole, the antenna is not turned over from positive θ to negative θ and the direction of the θ polarization vector does not change from positive to negative. A mode ±1 spiral has a phase rotation of 180º from φ rotation of 180º, but when we use a negative θ we did not turn over the antenna and phase remains unchanged. When we collect measurements on an automatic system that stores data as θ and φ polarization components and adds 180º to the phase of these components if negative θ (or 180º to 360º) are

measured, we need to use Huygens source polarization [(Eq. 1-37)] for linear polarization or remove the phase rotation of circular polarization before applying Eq. 13-1 or Eq. 13-2. Similarly, if we use the position of the antenna that gives the minimum phase error loss for a given reflector *f/D*, we need to convert to these polarizations and remove phase rotation with φ given the circular mode number before applying Eq. (8-7).

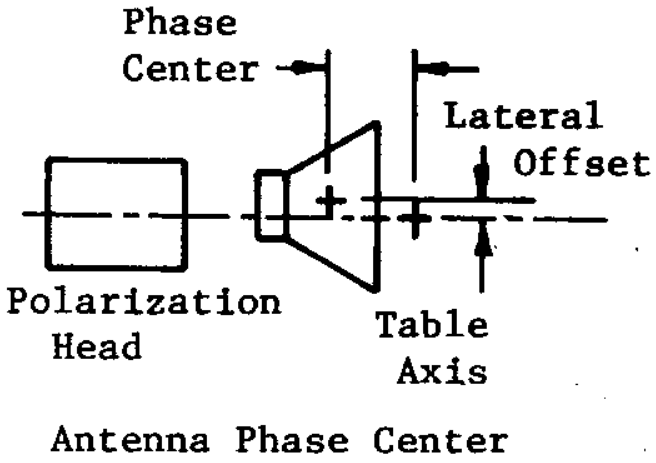

Figure 13-19 Antenna mounted on model tower positioner and phase center location relative positioner axes

In a manual measurement we move the antenna along the *z*-axis travel of the model tower positioner until its phase center is aligned with the table (azimuth) axis. For the position shown in Figure 13-19 (phase center behind the table axis), the sum of phases [Eq. (13-1)] is positive. We measure phase and calculate the lateral offset in the $\varphi = 0$ plane (*x*-axis) and $\varphi = 90^o$ plane (*y*-axis) to determine the separate components. If the positive axis direction is up as shown in Figure 13-19, the phase increases from the $-\theta$ position to the θ position for the lateral offset shown. Remember the positioner axis rotates CW for positive rotation, which is a CCW rotation along the antenna coordinate system (positive). A feed antenna may exhibit spherical aberration, which means it does not have a unique phase center but its location depends on the angles off boresight. We determine this movement by computing phase center at a number of pairs of θ positions using Eq. (13-1). When we use small values of θ, the denominator terms of Eqs. (13-1) and (13-2) multiply the errors of the phase measurements and reduce accuracy. The antenna may also exhibit astigmatism (Section 8-5) where the phase center location depends on φ. A mode 1 antenna has its extrema in orthogonal planes that usually occur in the *E*- and *H*-planes. We apply Eq. (13-1) in a number of planes defined by φ to determine astigmatism.

We need to detect whether phase has gone through multiple cycles, which it will for large values of phase center and lateral offset by adding phase change between measurements at small positioner steps. If we know before hand that the antenna is located significantly off the center of rotation, we should remove the phase change due to movement before calculation and then add it to the final result. We encounter this problem when we measure antennas on mockups where the antenna is also located off axis when we want to interpolate data to in-between angles and the antenna moves multiple cycles between measurement points. We remove the phase due to movement from the measurement, interpolate the data at new angles, and afterward add back the phase due to position.

We cannot apply Eq. 13-1 if the antenna has a pattern null at boresight because phase is ill-defined at this null. The solution is to find similar formulas using only measurements on one side of θ. We use measurements at an inner angle θ_1, an outer angle θ_2 (e.g. reflector half-subtended angle [Eq. (8-2)], and at an angle between (e.g. $\theta_c = (\theta_1 + \theta_2)/2$).

$$A = \sin\theta_2 - \sin\theta_c \quad \text{and} \quad B = \sin\theta_1 - \sin\theta_c$$
$$D = \cos\theta_2 - \cos\theta_c \quad \text{and} \quad C = \cos\theta_1 - \cos\theta_c$$
$$\text{Phase center} = \frac{\lambda(Ph_{1,c}A - Ph_{2,c}B)}{360(AC - BD)} \tag{13-3}$$
$$\text{Lateral offset} = \frac{\lambda(Ph_{2,c}C - Ph_{1,c}D)}{360(AC - BD)}$$

We average the phase center and lateral offset over all measured φ angles to serve as an initial guess for an optimization routine using phase error loss for a given reflector *f/D* as the cost function to determine a unique phase center. To use the simple cost function for a mode 1 feed [Eq. (8-7)], we remove the higher order mode phasing due to φ rotation before applying the equation. This operation enables an optimization search to determine phase center. However, the phase error loss found by this operation is not the correct when the actual beam-peak occurs off-boresight in the reflector pattern. Amplitude taper loss and spillover loss are unaffected by this operation and are correct. We must do a full pattern analysis including the reflector using physical optics to determine actual gain. For a mode 1 circularly polarized feed we remove the phasing due to φ rotation by projecting the measurements on a unit circularly polarized vector similar to the projection on to Huygens polarization for a linear antenna. Projection involves taking the scalar (dot) product with the complex conjugate (Section 1-11). The feed antenna could have a ring focus for use with reflectors with the vertex expanded into a ring similar to the displaced axis dual reflector (Section 8-16) and we use Eq. (13-3) in various φ planes to determine this lateral offset in all planes (ring focus).

13-5.2 Alignment of model tower

After moving the horizontal travel of the positioner until the table axis is aligned with phase center, we must determine its location on the antenna. A transit theodolite placed off to the side can be used to determine the location of the center of rotation about the table axis on the antenna. A second method is to mount a laser with its beam aligned with the table axis and the laser spot on the antenna shows the center of rotation and phase center.

A model tower uses a dielectric column and its mounting to the table can be misaligned and produce significant measurement error. Figure 13-20 show two types of misalignments that can be detected by electrical measurements. The horizontal axis of the polarization head should intersect the vertical table axis. A positioner whose axes do not intersect has lateral offset and our measurement of antennas will always exhibit lateral offset. Of course, the lateral offset of the antenna will add or subtract from this lateral offset depending the relative φ angle of measurement. We measure lateral offset, rotate φ 180º and repeat the lateral offset measurement. The antenna lateral-offset shifts sides and sign while the positioner offset remains constant. We add the two measurements and divide by 2 to find positioner offset. We can correct the positioner lateral offset by shimming the tower at its mounting point. The dielectric tower mount seldom has alignment pins and the tower can rotate slightly in the bolt clearance holes. Figure 13-20(*b*) illustrates an exaggeration of this effect. The table travel axis does not align with the polarization head axis. Our measurement of lateral offset changes when we move the model tower travel. By repeating the lateral offset measurement at different travel positions, we detect this problem. We may have to rely on mechanical alignment measurement techniques to align the positioner.

One effect is distortion of the dielectric tower due to the weight of the antenna. The weight may bend the tower forward so that the polarization head is no longer orthogonal to the table axis. Unless the tower has an elevation axis, the antenna boresight cannot be pointed along the source axis and we measure boresight along a ring. A second problem with a heavy antenna is that some model towers are made in a helix. The weight causes rotation in the helix because the tower is weak at the joint where one turn of the helix joins the next turn. Reflection of a laser beam to the back wall from a mirror mounted on the front surface readily shows both types of flexure.

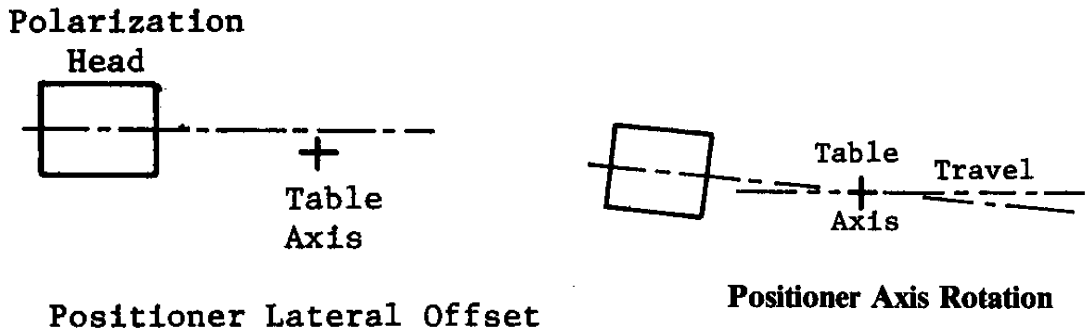

Figure 13-20 Misalignments of model tower positioner

13-6 Gain Measurement

We compare the powers received by an antenna with a known gain to that of the antenna under test (AUT) to determine gain. Given a source gain g_s, and wavelength λ, the ratio of received power to transmitted power is

$$\frac{P_{AUT}}{P_{in}} = g_{AUT} g_s \left(\frac{\lambda}{4\pi R_{AUT}} \right)^2$$
$$\frac{P_{ST}}{P_{in}} = g_{ST} g_s \left(\frac{\lambda}{4\pi R_{ST}} \right)^2 \qquad (13\text{-}4)$$

for the AUT and gain standard (ST). We compare the output powers and cancel like terms.

$$\frac{P_{AUT}}{P_{ST}} = \frac{g_{AUT}}{g_{ST}} \left(\frac{R_{ST}}{R_{AUT}} \right)^2 \quad \text{or} \quad g_{AUT} = g_{ST} \frac{P_{AUT}}{P_{ST}} \left(\frac{R_{AUT}}{R_{ST}} \right)^2 \qquad (13\text{-}5)$$

Most of the time we want the two distances to be the same because range reflections can alter the $1/R^2$ transmission characteristic from the free space path loss formula. Converted to decibels Eq. (13-5) becomes

$$G_{AUT,dB} = G_{ST,dB} + 10\log\left(P_{AUT} / P_{ST}\right) + 20\log(R_{AUT} / R_{ST}) \qquad (13\text{-}6)$$

We calibrate an automated measurement by adding an operation where we measure the gain standard and the program adjusts all measurements in the file to be gain.

Example An antenna's gain is measured with respect to a standard gain horn with 16 dB gain as -5 dB. The distance from the source antenna to the AUT is 33.5 ft., whereas the distance to the gain standard is 31.1 ft. The gain of the AUT is $G_{AUT,dB}$ = 16 – 5 +20 log(33.5/31.1) = 11.65 dB

Cable Connected to Antenna Gain Ripple due to Cable Mismatch

When a cable is connected to an antenna and the gain is measured, it will show a ripple in the frequency domain due to the cable connector mismatch. The mismatch of the cable connected to the antenna cannot be separated from the antenna by looking at the time domain. The ripple in the response is due to the reflected power loss of the combination mismatch.

We determine the length of the cable by noting the frequency separation of the nulls. The reflection of the antenna/cable connector either adds or subtracts from the second cable connector mismatch. Because this is a reflection we note that the response repeats on a Smith chart at half wavelength intervals. Given the frequency separation F_s the cable length is a half wavelength at this frequency.

$$Length = \frac{c}{2F_S\sqrt{\varepsilon_r}}$$

Example The frequency difference between nulls is 100 MHz for a Teflon filled (dielectric constant = 2.1) cable. When we insert these values in the equation above, the length equals 40.7 inches.

The maximum VSWR given the two mismatches of the cable connector and antenna/cable connector combination is the product of two VSWR's and the minimum VSWR is the ratio.[i] We compute the VSWR from the return loss by first computing the voltage reflection coefficient.

$$\rho = 10^{-\mathrm{Re}turnLoss/20} \qquad \mathrm{VSWR} = \frac{\rho+1}{\rho-1}$$

The product and ratio of the two mismatches separated in distance VSWR's are given by V_X (maximum) and V_N (minimum). We compute the reflected power loss for each case by

$$Power\ Loss(dB) = 10Log\left[1-\left|\rho\right|^2\right] \text{ where } \rho = \frac{VSWR-1}{VSWR+1}$$

The frequency response ripple is the difference of these two Power Losses for maximum and minimum VSWR. The amount of ripple due to a cable connector mismatch depends on the antenna/cable connector combined return loss. The scales below show the ripple due to cable connector mismatch for fixed values of the antenna/cable connector mismatch. Generally, the antenna mismatch dominates the combination of cable mismatch and antenna.

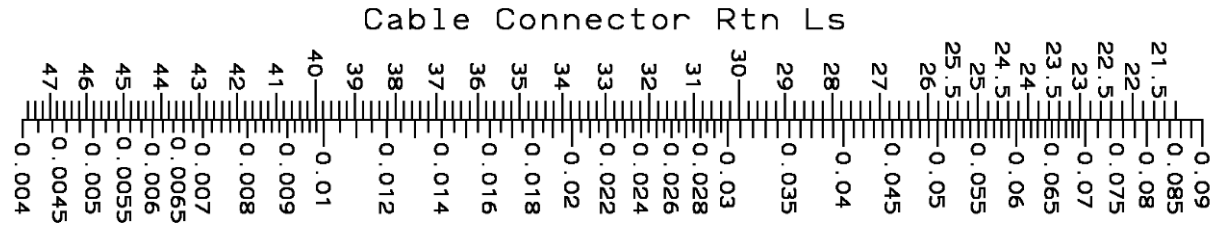

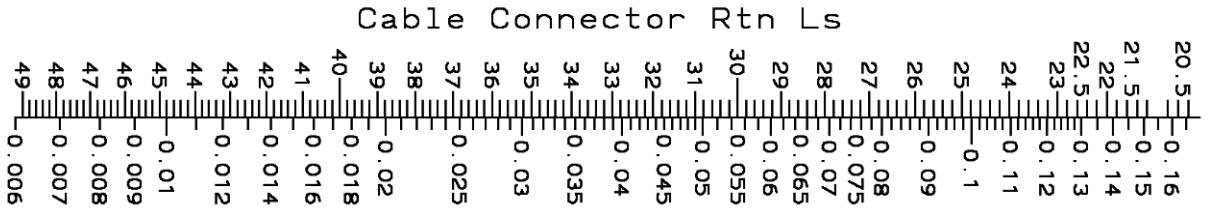

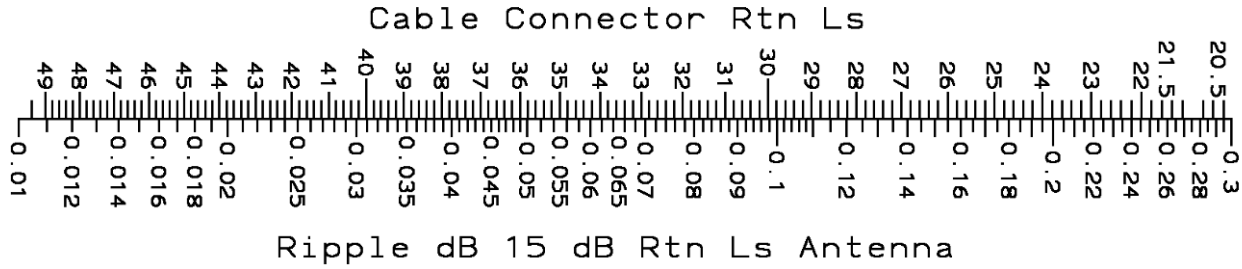

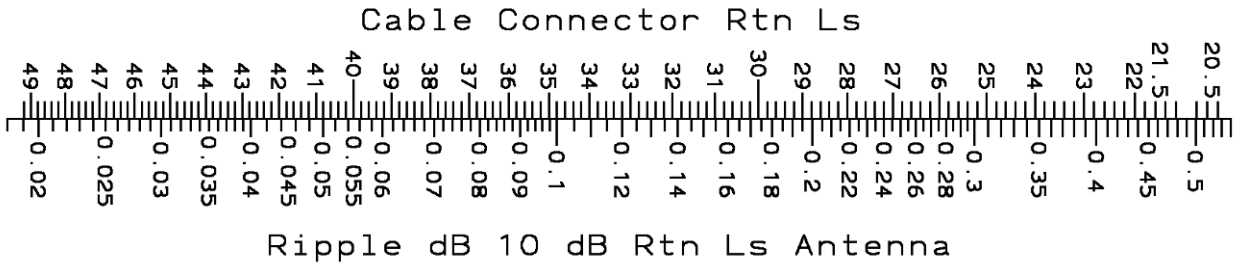

If we assume each cable connector has the same mismatch, we find the individual connector mismatch from cable measurement. The cable measurement with have a similar frequency ripple response as above and we use the minimum return loss to determine the return loss of the individual connector mismatches.

The ripple due to the connector mismatch can be removed in the time domain using a filtering window provided a sufficient frequency range is available to resolve the far connector on the cable. After being converted back to the frequency domain, the response ripple will be removed.

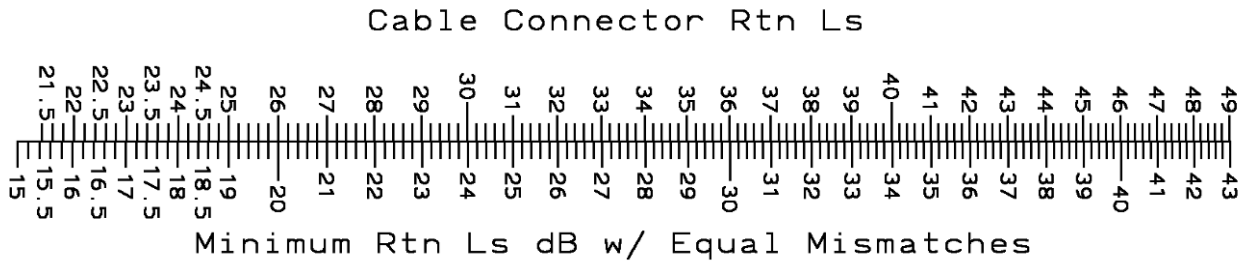

[1] George L. Ragan, ed., *Microwave Transmission Circuits,* McGraw-Hill, 1948, p. 554

Circularly Polarized Antenna Gain Measurement using Linear Polarization

One method of measuring a circular polarized antenna is to use a linear source antenna. By measuring the gain relative to a linear polarized gain standard and noting the axial ratio by rotating the source, the gain correction is given by the scale below. For example, an antenna with a 3 dB axial has a circular gain 1.64 dB above the measured value as a linear antenna at the peak of the CP response. The scale below is the gain correction factor given by Eq. (1-47).

The other method is to measure the Theta and Phi (co-pol. and cross-pol. Huygens source) components which have been calibrated to linear gain standards and compute the circular components (see section 1-11.1).

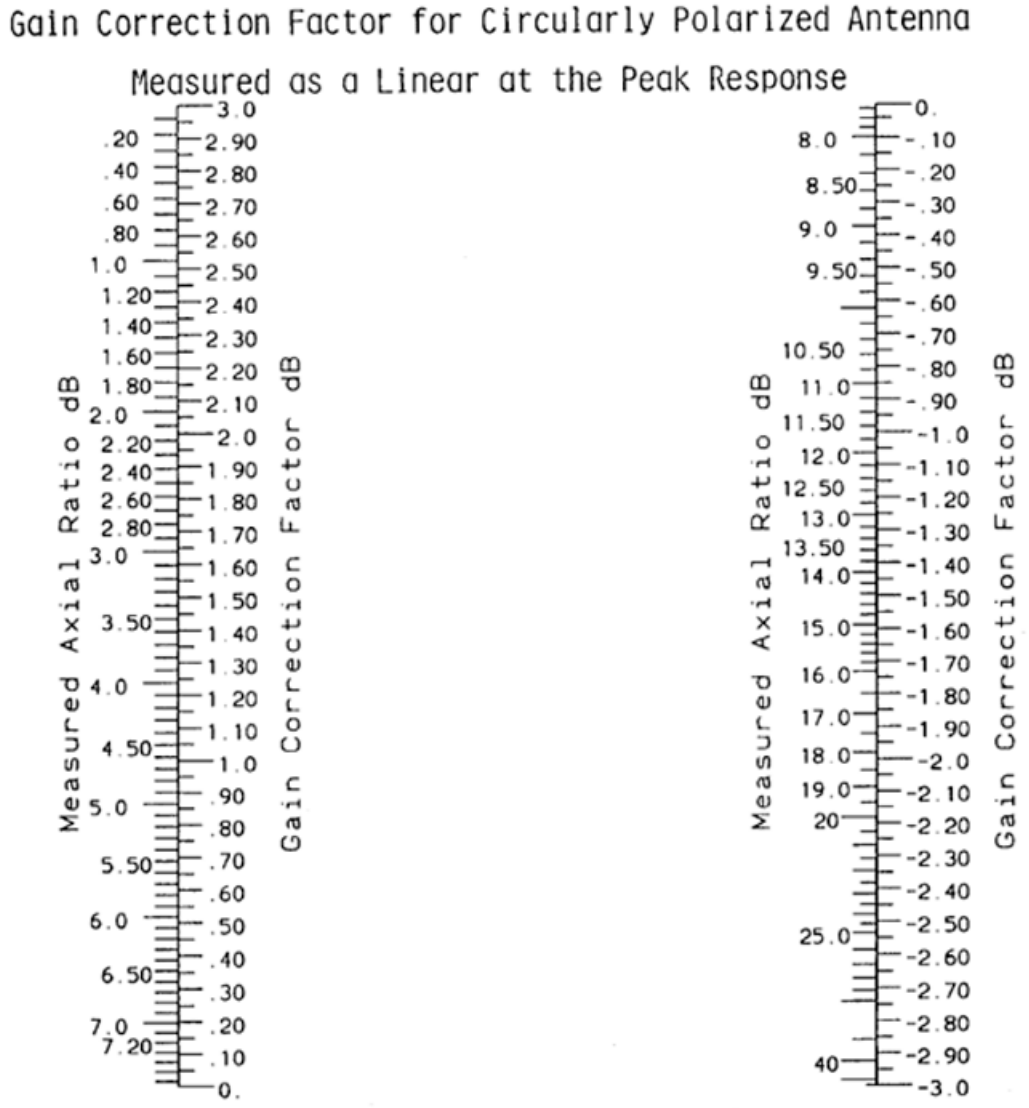

Scale 13-8 Gain Correction Factor of CP antenna Measurements using Linearly Polarized Standards

13-6.1 Two identical antenna gain standard measurement

We use path loss to determine the value of a gain standard. Two mechanically identical antennas can be used to find gain. First measure the return loss of the two antennas to verify that they are identical. We rearrange [Eq. (1-9)] using the same gain for the transmitting and receiving antennas.

$$G_{ST} = \left(K_U + 20\log(fR) - path\ loss(dB)\right)/2 \qquad (13\text{-}7)$$

The constant K_U depends on the range units [see Eq. (1-9)] for frequency f in MHz. In Eq. (13-7) path loss is a positive number. These measurements will not work on a ground plane range or in a tapered chamber because the significant level of reflections change the effective gain of the source antenna. We have the same problem with the three antenna measurement.

At low frequencies we must measure the antennas on an elevated range. The ground reflection either adds or subtracts from the direct signal. Figure 13-7 shows the expected path loss ripple versus downrange for a particular range. The peak-to-peak range is about 70 ft. for a wavelength of 1/3 ft. We need to move the antennas closer

together to decrease the range difference from peak-to-peak, but still be in the far field of the antennas. By making measurements at many distances, we can average out the downrange ripple due to ground reflection. We call this an *extrapolation measurement*. The extrapolation technique allows near field measurements because the gain curve can be extrapolated to the correct value when the data is fit to an equation. It will be necessary to analyze the downrange ripple response on the range to determine how many measurements will be needed over what distance.

13-6.2 Three antenna gain standard measurement

We can use any three antennas that operate at the same frequency and make path loss measurements between them and to eliminate the requirement for identical antennas to calibrate gain standards. One antenna is used to transmit only, one receiving only, and one both transmitting and receiving. If we move one antenna from the receiving end to the transmitting end of a tapered chamber, its gain changes due to wall reflections and this is why we cannot calibrate gain standards in a tapered chamber (or on a ground plane range). We measure the transmission loss three times: S_{21} antenna 1 to antenna 2, S_{31} antenna 1 to antenna 3, and S_{32} using a network analyzer calibrated for transmission loss. We calculate a gain factor $GF = K_U + 20\log(fR)$ and separate the three transmission measurements into the gain of each antenna.

$$\begin{aligned} G_{1,dB} &= (S_{21,dB} + S_{31,dB} - S_{32,dB} + GF)/2 \\ G_{2,dB} &= (S_{21,dB} - S_{31,dB} + S_{32,dB} + GF)/2 \\ G_{3,dB} &= (-S_{21,dB} + S_{31,dB} + S_{32,dB} + GF)/2 \end{aligned} \tag{13-8}$$

13-6.3 Three antenna gain-polarization standard measurement

Equation (13-8) assumes that the three antennas have insignificant cross polarization and their polarizations were rotated to the peak response. That is, probably linearly polarized horns. We need six measurements to separate the two polarization components of the three antennas. We measure first with the antennas co-polarized and then rotate the receive antenna by 90º CCW and repeat the measurement. The R antenna is receiving only, T transmitting only, and S transmitting and receiving with horizontal (co-pol) response R_X and vertical (cross-pol) response R_Y, and so on. The six voltage measurements (complex) are designated:

D_{RT} – direct transmitting only to receiving only – both horizontally polarized
P_{RT} – transmitting only to receiving only with receiving rotated 90º CCW
D_{RS} – direct transmitting/receiving to receiving only – both horizontally polarized
P_{RS} – transmitting/receiving to receiving only with receiving rotated 90º CCW
D_{ST} – direct transmitting only to transmitting/receiving – both horizontally polarized
P_{ST} – transmitting only to transmitting/receiving with transmitting/receiving rotated 90º CCW

These measurements work on both linearly and elliptically polarized antennas. We convert these measurements into pseudo left- and right-hand components.

$$\begin{aligned} S_{RT} &= (D_{RT} + jP_{RT})/2 \text{ and } T_{RT} = (D_{RT} - jP_{RT})/2 \\ S_{RS} &= (D_{RS} + jP_{RS})/2 \text{ and } T_{RS} = (D_{RS} - jP_{RS})/2 \\ S_{ST} &= (D_{ST} + jP_{ST})/2 \text{ and } T_{ST} = (D_{ST} - jP_{ST})/2 \end{aligned} \tag{13-9}$$

We compute the receiving only antenna components.

$$\begin{aligned} R_N &= \sqrt{S_{RT}S_{RS}/S_{ST}}/\sqrt{2} \text{ and } R_P = \sqrt{T_{RT}T_{RS}/T_{ST}}/\sqrt{2} \\ R_X &= j(R_N + R_P) \text{ and } R_Y = R_N - R_P \\ &\text{If } |R_X| \prec |R_Y|,\ R_X = j(R_N - R_P) \text{ and } R_Y = R_N + R_P \end{aligned} \tag{13-10}$$

We use similar expressions for the transmitting/receiving antenna components.

$$S_N = \sqrt{S_{RS}S_{ST}/S_{RT}}/\sqrt{2} \text{ and } S_P = \sqrt{T_{RS}T_{ST}/T_{RT}}/\sqrt{2}$$
$$S_X = j\left(S_N + S_P\right) \text{ and } S_Y = S_N - S_P \quad (13\text{-}11)$$
$$\text{If } |S_X| \prec |S_Y|,\ S_X = j\left(S_N - S_P\right) \text{ and } S_Y = S_N + S_P$$

The transmitting only antenna has the conversion expressions.

$$T_N = \sqrt{S_{RS}S_{ST}/S_{RT}}/\sqrt{2} \text{ and } S_P = \sqrt{T_{RS}T_{ST}/T_{RT}}/\sqrt{2}$$
$$T_X = j\left(T_N + T_P\right) \text{ and } T_Y = T_N - T_P \quad (13\text{-}12)$$
$$\text{If } |T_X| \prec |T_Y|,\ T_X = j\left(T_N - T_P\right) \text{ and } T_Y = T_N + T_P$$

We convert these components to decibels and add the factor *GF*/2 to find the gain (dB). We use the voltage components to compute the right- and left-hand polarization components [Eq. (1-39)] and the tilt of the polarization ellipse.

13-7 Efficiency of small antennas

We compute efficiency of moderate sized antennas by comparing gain and directivity. If we measure the antenna at a discrete set of angles that covers the radiation sphere, both gain and directivity have the same error when the peak response is missed. The integral of the pattern over the radiation sphere has a second-order error if the peak of the beam is missed. These operations find efficiency with a second-order error.

Small antennas have wide and ill-defined patterns that radiate in all directions. It is difficult to mount the antenna without seriously affecting its pattern. We circumvent these problems by measuring the antenna in a confined cavity or space to determine its losses or *Q*. The small antenna has a narrow bandwidth, which allows the use of the cavity. The Wheeler cap measurement uses reflection measurements using a network analyzer to determine losses. We must mount the antenna on a ground plane to restrict its pattern. The ground plane does not affect its efficiency, but it will change its impedance match. Many small antennas are operated when mounted on a ground plane. Second place a metal cap over the antenna and re-measure the input impedance match. This metal cap should be at least 1/6 λ away from the antenna. This metal cap eliminates radiation and we measure the material losses.

We need to know the circuit model of the antenna near resonance because it affects the calculation of efficiency.

Model 1, resistances: reflections on constant resistance circles on Smith chart – series circuit

$$\eta = \frac{R_{rad}}{R_L + R_{rad}} \quad (13\text{-}13a)$$

Model 2, conductances: reflections on constant conductance circles on Smith chart – shunt circuit

$$\eta = \frac{G_{rad}}{G_L + G_{rad}} \quad (13\text{-}13b)$$

Model 3, reflections on constant radius on Smith chart

$$\eta = \frac{\left|S_{11,WC}\right|^2 - \left|S_{11,FS}\right|^2}{1 - \left|S_{11,FS}\right|^2} \quad (13\text{-}13c)$$

We need to observe the impedance frequency response on the Smith chart to determine which version of Eq. (13-13) we use to compute efficiency. Some cases fail to follow any of the circuit models and the efficiencies, calculated by the three methods, are slightly different.

Figure 13-21 illustrates using waveguide techniques to measure efficiency of a small antenna independent of a circuit model. We need to build a waveguide whose cut-off frequency is below the operating frequency of the antenna.

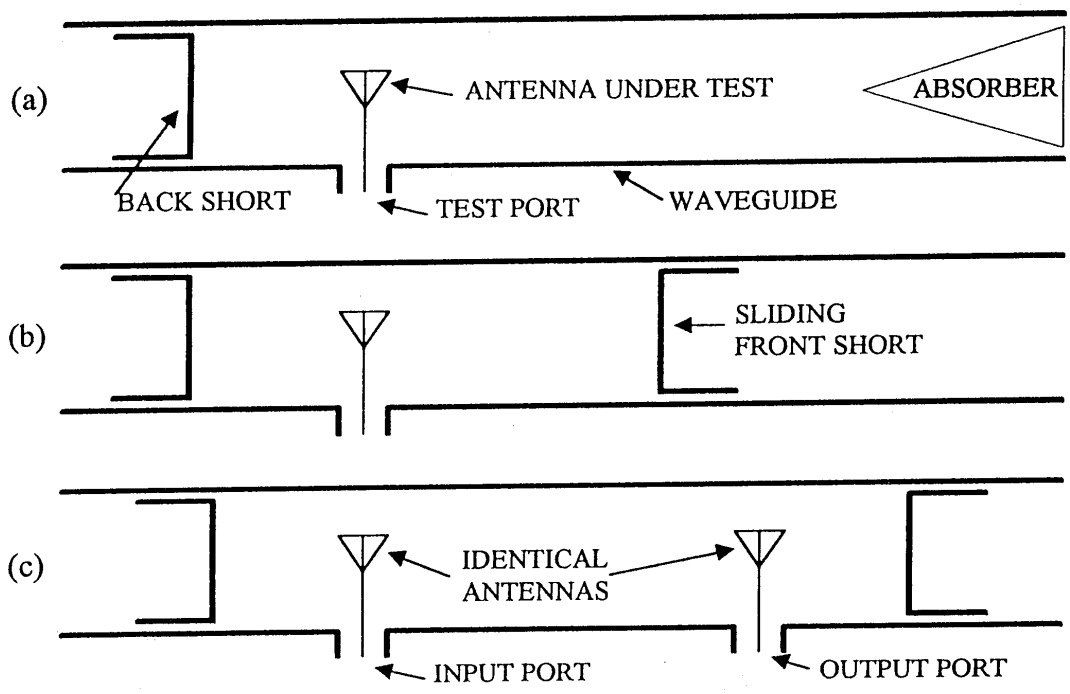

Figure 13-21 Rectangular waveguide efficiency measurements of antenna

Method 1: Reflection measurements only

1) Measure the antenna reflection in free space $S_{11,FS}$
2) Place antenna in rectangular waveguide and use it to feed the waveguide with a load on the end, Figure 13-21*a*. Adjust the back-wall until $S_{11,FS} \approx S_{11,WG}$
3) Replace the waveguide load with a short and measure $S_{11,WGS}$ for various positions of front short and compute efficiency

$$\eta = \sqrt{\left|S_{11,WGS} - S_{11,WG}\right|_{MAX}} \sqrt{\left|S_{11,WGS} - S_{11,WG}\right|_{MIN}} \tag{13-14}$$

Method 2: Transmission test measurement, Figure 13-21*c*

1) Install identical antennas under test in waveguide operating above cut-off
2) Move sliding shorts to give physical symmetry in waveguide
3) Measure $S_{11,WGT}$, $S_{21,WGT}$, and $S_{22,WGT}$. Verify $S_{11,WGT} = S_{22,WGT}$ for symmetry and compute

$$\eta = \frac{\left|S_{21,WGT}\right|^2}{1 - \left|S_{11,WGT}\right|^2} \tag{13-15}$$

13-8 Time-domain methods in antenna measurements

We operate receivers and network analyzers in the stepped-frequency mode and measure antennas over a large frequency range easily. We transform these measurements by using the fast Fourier transform (FFT) or chirp-Z transform into the time (distance) domain either internally in the analyzer or externally from a table of measurements to determine antenna range multipath problems. By applying a software time (distance) gate to the data, we eliminate multipath reflections on the antenna range and reduce measurement errors. The transform of a stepped frequency response is a Fourier series expansion that has multiple repeating responses. The time between repeating responses (alias free range) is related to the frequency step Δf,

$$\text{alias free time (nsec.)} = \frac{1}{\Delta f\,(GHz)} \tag{13-16}$$

Given the speed of light, 1-ft/nsec (0.3m/nsec), we compute the alias free range.

$$\text{alias free range (ft)} = \frac{1}{\Delta f\,(GHz)}$$
$$\text{alias free range (m)} = \frac{0.3}{\Delta f\,(GHz)} \qquad (13\text{-}17)$$

Example Determine frequency step to allow detection of multiple reflection at 30m. To allow clear resolution at 30m, we use a frequency step to give about 75m of alias free range or 37.5m on both sides of $t = 0$. By using Eq. (13-17), $\Delta f = 0.3/75 = 0.004$ GHz = 4 MHz.

The total frequency range determines the resolution, where two signals appear separated, of the multipath on the range. ΔT = 1/(frequency range) or ΔT(nsec) = 1/[frequency range (GHz)]. The distance resolution is

$$\Delta\text{Distance (ft)} = \frac{1}{\text{Frequency range (GHz)}}$$
$$\Delta\text{Distance (m)} = \frac{0.3}{\text{Frequency range (GHz)}} \qquad (13\text{-}18)$$

Example To determine the multipath location within 10 cm, we need measurements over the frequency range = 0.3/0.1 = 3 GHz. If we combine this with the example above that has 75m alias free range, we need to measure 751 frequencies. A measurement with only 101 frequencies over 400 MHz could resolve distance only to 75 cm.

For a reflection measurement the signal travels twice the distance and the alias free range Eq. (13-17) is half and the resolution is also half. We use these measurements to locate problems in a cabling system. We can convert the time-domain impulse response to a step response by integrating the impulse response. When we measure within a cable, we convert the integrated time impulse response and convert the reflection coefficient to resistance. Reactance has no meaning in the time-domain. This is the time-domain reflectometer (TDR) response used to measure resistance changes in a transmission line.

If there is a ripple in the frequency domain, it is due to two signals separated by a distance. For a transmission measurements the distance is equal to the wavelength of the delta frequency, while a reflection measurement is half that value. The ripple in patterns is covered in Section 3.1a.

13-8.1 Distance to fault tests

The cables on an antenna range or a cell-site base station can be tested using a stepped frequency reflection measurement. The tests are called *frequency domain reflectometry* and can be performed using a small portable instrument. The instrument measures S_{11} over a stepped frequency range, zero pads the measurement to 2^N points, and uses the FFT to convert to time (distance) domain. When the range cables or base station is completed and checked out, the instrument separates the reflection at each junction to show they are properly connected. For the base station the transmitting antennas are checked for excessive impedance mismatch in the as-mounted configuration including cable interaction. Periodically, the base station is measured to see if any changes are occurring. These measurements can be automated and performed on a schedule to detect problems and order repairs.

A reflection measurement travels twice the distance of a transmission measurement on an antenna range. Given the dielectric constant of the cable ε_r and the velocity of light c, we determine the frequency step

$$\text{Distance range} = \frac{c}{4\Delta f\sqrt{\varepsilon_r}} \quad \text{or} \quad \Delta f = \frac{c}{4\sqrt{\varepsilon_r}\,(\text{Distance range})} \qquad (13\text{-}19)$$

The total frequency range of measurements determines the resolution

$$\text{Distance resolution } \Delta D = \frac{c}{2\Delta f\,2^N\sqrt{\varepsilon_r}} = \frac{c}{2\sqrt{\varepsilon_r}\,(\text{Frequency range})} \qquad (13\text{-}20)$$

Example Cable run of 100-ft with dielectric $\varepsilon_r = 2.1$, we use Eq. (13-19) to compute the frequency step required: $\Delta f = 10^9/(4\sqrt{(2.1)}100) = 1.725$ MHz. We use Eq. (13-20) to determine the step frequency range given the desired distance resolution. Assuming an airline: 24 in. needs 246 MHz bandwidth; 12 in., 492 MHz; 6 in., 984 MHz, 3 in., 1967 MHz; 1 in., 5.9 GHz, and so on.

To determine the reflection at a given point on the cable, we increase S_{11} by twice the loss to that position because the instrument computes the cable length and we enter the loss per length.

13-8.2 Time-gated measurements

We reduce multipath by time-gating the measurement by either using a hardware or software gate. The AUT and source antennas need to have sufficient bandwidth to allow radiation of the whole frequency range or an equivalent bandwidth given the pulse width of the hardware gate. We could use the fast Fourier transform (FFT) or chirp-Z transformer on the frequency response and gate the response in software. First we need to center the response on the propagation time through the chamber to the AUT by adding a phase slope (group delay) to the measurements. Given the difference between the range and reference channel distances d and the frequency f, we add phase to each measurement to remove the group delay negative slope. Phase = $360^o d(f)/c$ before calculating the transform and zero will be centered at d. The distance of the multipath relative to the direct signal determines the alias free range and the required measurement Δf by using Eq. (13-17).

$$\text{alias free time (nsec.)} = \frac{\text{\# of Frequencies - 1}}{\text{bandwidth}(GHz)} \tag{13-21}$$

We form a window on the response around $t = 0$ (distance = 0) to remove the multipath signals and compute the inverse transform to calculate the antenna response free of multipath. If necessary, we add the antenna range distance group delay phase shift to the data: Phase = $-360^o d(f)/c$ to return it to its original phase slope.

If we use a uniform amplitude window on the distance data, we introduce Gibbs ripple to the transformed frequency response data. A uniform amplitude window has the -13.2 dB sidelobes and equivalent pass band ripple that alters the data. We need a tapered filter window to reduce these effects. We could use a Chebyshev or sampled Taylor distribution digital filter to reduce the Gibbs ripple. The network analyzer with the software gate option uses an elliptic (Cauer) filter that has small ripples in the pass band and a rapid fall-off in the filter skirts to uniform amplitude sidelobes. To reduce the Gibbs ripple, the filter tapers the time responses outside the gate over the whole FFT range. Both the network analyzer receiver and commercial measurement software use the same filters. Table 13-1 lists the filter types and their characteristic given the measurement bandwidth, *BW* (GHz).

Table 13-1 Characteristics of software gate digital filters with measurement bandwidth, *BW* (GHz).

Gate Shape	Minimum Gate Width (-6 dB Points)	0 to -6 dB Rise/Fall Time	0 dB to Stopband Rise/Fall Time	Passband Ripple dB	Maximum Stopband Sidelobe Level dB
Minimum	1.2/*BW*	0.6/*BW*	1.2/*BW*	±0.40	-24
Normal	2.8/*BW*	1.4/*BW*	2.8/*BW*	±0.04	-45
Wide	8.0/*BW*	4.0/*BW*	8.0/*BW*	±0.02	-52
Maximum	22.4/*BW*	2.8/*BW*	22.4/*BW*	±0.01	-80

The distance to the source of multipath determines which filter is required. If we need to use the Minimum filter because the multipath distance is close, we introduce conversion errors. It may be better to increase the measurements bandwidth provided the antenna VSWR is stable over this frequency range. It is important that the sum of the phase center movement versus frequency of both the transmitting and receiving antenna combined with antenna movement during the test does not move the antenna outside the hardware or software gate. Second, it is assumed that the antennas will have reasonable responses across the frequency range. When the data is transformed back to the frequency range, the data near the band edges will be altered by these operations and become inaccurate. We need to measure across a larger bandwidth so that the center portion will still be accurate. We need to eliminate a percentage of the frequency sweep on both edges, Table 13-2 as inaccurate. Although the Minimum gate has the smallest frequency region of inaccurate conversion on both sides of the gated band, the errors have been spread throughout the band.

Table 13-2 Frequency data to avoid on each edge after gating

Gate Shape	Percentage of frequency sweep To avoid on each edge
Minimum	1%
Normal	5%
Wide	10%
Maximum	20%

The software gate has the advantage of being applied after measurement and can be adjusted, whereas measurements with the hardware gate applied cannot be altered in post-processing.

13-9 Compact Range

The compact range uses a paraboloidal reflector to transform a incident spherical wave into a plane wave (collimated) beam that illuminates the AUT as shown in Figure 13-22. An offset fed reflector eliminates feed blockage, but this introduces cross-polarization and amplitude taper vertically across the AUT. The use of a large $f/D \approx 1$, reduces the cross-polarization and edge taper [Eq. (8-3)] to less than 0.55 dB [Scale 8-2]. Scattering from the feed antenna and the rim of the reflector introduce additional cross-polarization and ripple.

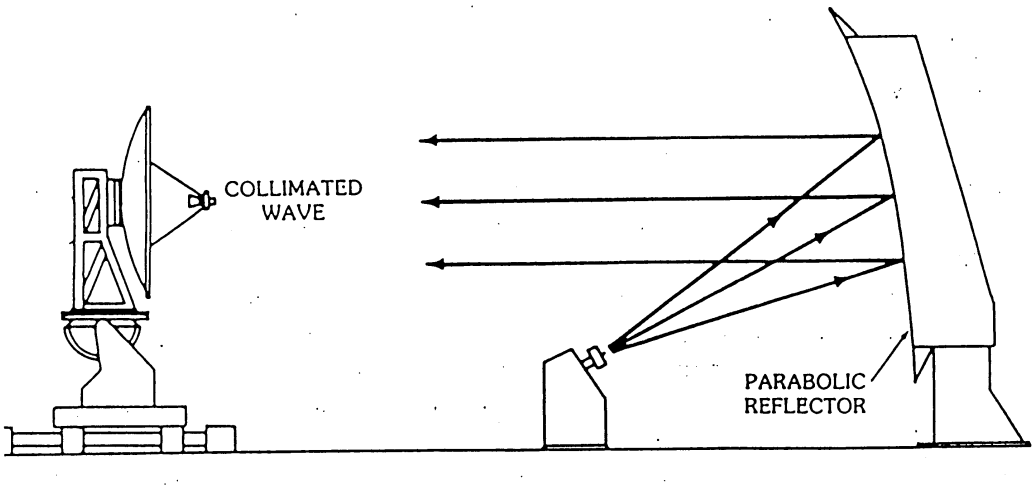

Figure 13-22 Compact range uses paraboloidal reflector to collimate beam

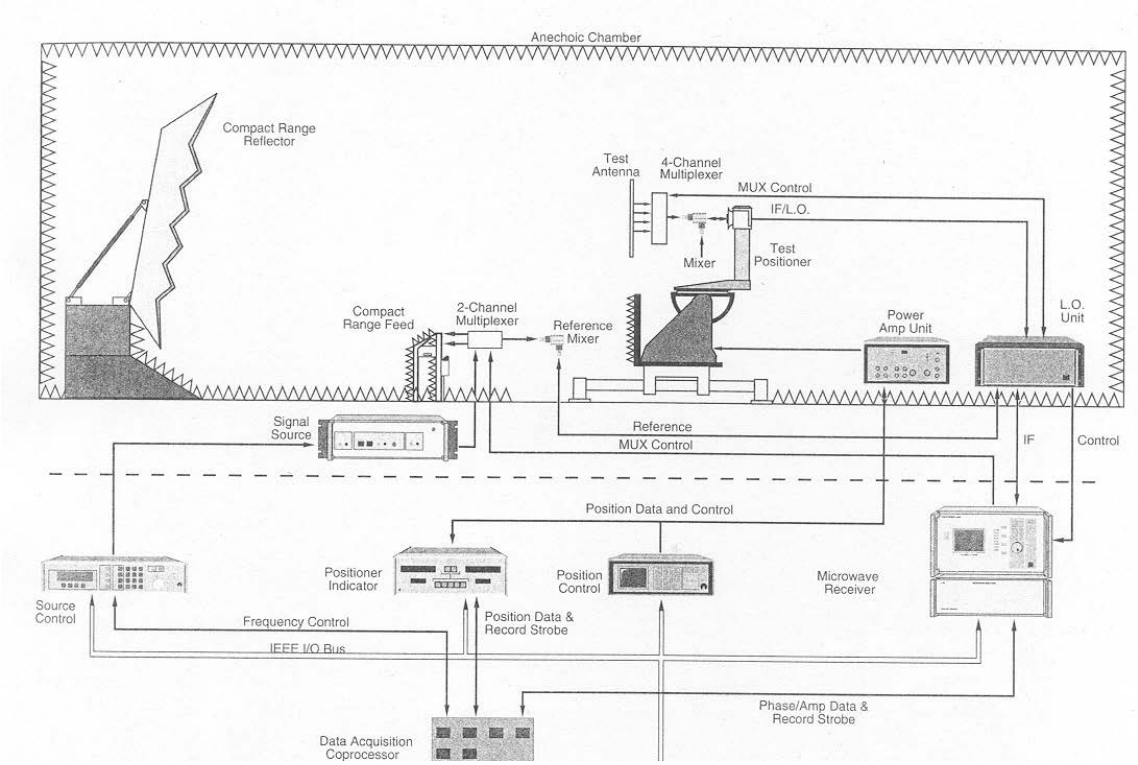

Figure 13-23 Instrumentation of compact range

To achieve a flat amplitude across the quiet zone, a wide beamwith feed is used. Given the diameter of the quiet zone, D and the reflector focal length f, we find the beamwidth from [Eq. (8-2)] $\approx (57.2 - 0.0044\psi_f^2)^o/(f/D)$ where ψ_f is the feed pointing in degrees [1]. Figure 13-23 shows serrations on the main reflector that reduce the scattering from the rim by scattering it in all directions. A second approach uses a rolled edge, Figure 13-24, to reduce rim diffraction. Both methods work when the length of the serrations is at least 4λ. It is claimed that the rolled edge works better at low frequencies. Offset feeding the reflector introduces cross polarization given approximately as [1],

$$20\log\left(\frac{\sin\psi_f}{4f/D}\right) \quad \text{dB} \tag{13-22}$$

which ranges from -25 to -30 dB.

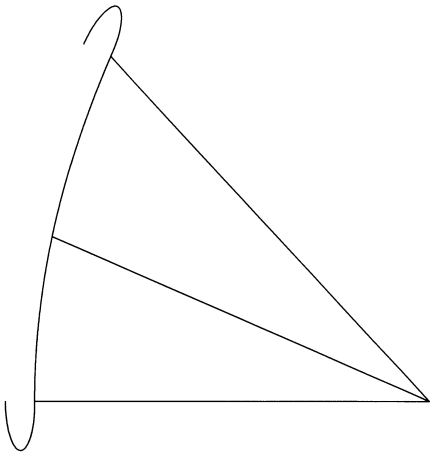

Figure 13-24 Rolled edge to reduce rim scatter from compact range reflector.

The aperture of the main reflector has both amplitude and phase ripples across the AUT. Not only is the edge treatment important but the surface RMS. For example, a 0.01λ RMS produces ±0.25 dB ripple [3] and because the wave travels across the deviations twice, the phase RMS is 7.2º. We use a Gaussian distribution for this phase deviation. Systematic deviations across the main reflector lead to large phase variations [3]. Hand rework of the reflector was required to randomize the variations and reduce the phase variation. Edge diffraction is an interfering signal that produces a sinusoidal variation across the aperture in both amplitude and phase. Fortunately, we measure large apertures that integrate the aperture distribution and average out its variation. The AUT is in the near field of the main reflector and we must calculate coupling between the two antennas [Eq. (1-55) using fields and currents or Eq. (8-29) between radiated fields] to analyze these cases. When we measure gain using substitution, the standard gain averages the fields over a smaller aperture that leads to measurement error. Wide beam small antennas integrate less of the aperture fields. If it is mounted offset on a larger ground plane, it acts as a field probe measuring the aperture field variations. Higher gain antennas have lower measurement errors on a compact range.

Two types of dual reflector antennas are used to reduce cross polarization by tilting the feed and subreflector axis by the Mizugutch angle (Section 8-17). One method uses an offset Gregorian arrangement where the subreflector and feed are located below the chamber floor in a separate room. The signal propagates through a slot to the main reflector. The slot blocks the direct feed illumination of the test article and the edge diffraction of the subreflector. Of course, the size of the slot limits the low frequency because waves diffract from its edges that increases as we lower the frequency. The second dual reflector compact range uses a Dragonian dual-reflector (Figure 8-22) (Section 8-18). Direct feed illumination is a problem because the test article is located in the front hemisphere of the feed beam. Baffles covered with absorber or hardware gating prevents this illumination. The long effective focal-lengths of either dual-reflector antenna reduce the edge taper of the single reflector range. The Gregorian dual-reflector has been built with rolled edges on both reflectors. The Dragonian dual-reflector system utilizes serrations. Straight serrations reduce the cross polarization to about -40 dB with a ±0.5 dB aperture ripple and ±5º phase ripple. By curving the edges [2] the cross polarization can be reduces to less than -43 dB and the aperture ripple reduced to ±0.3 dB with ±2º phase ripple.

The instrumentation on this range is arranged similar to normal anechoic chambers. The source antenna is shown with a multiplexer to feed two orthogonal polarizations. Similarly, a multiplexer is placed on the receiving antenna to allow sequenced measurements of multiple ports on the AUT. The usual setup locates the reference channel mixer on a coupler connected directly to the transmitter cable at the source antenna. In this setup only the AUT positioner is moved during measurement, but a second positioner is often used on the source mount to rotate its polarization. We cover the source tower and parts of the positioner with absorber to reduce multipath. Figure 13-23 shows the AUT positioner mounted on rails to allow movement in the chamber to allow movement to the best the quiet zone across the antenna given frequency.

[1] Boumans, Marcel, Influence of range geometry and feed characteristics on compact range system level performance, AMTA 2000.
[2] Hartmann, Jürgen and Dietmar Fasold, Advanced Serration Design for Compact Ranges with UTD, AMTA, 2000.
[3] Griffin, W. R., Jr., and Roger Silz, Non-random reflector surface effects on compact range performance, AMTA, 2000.

13-10 Planar Near-field

Section 12-9 showed how planar near-field measurements can be used to find feeding errors in a planar array. This involved a holographic technique where the phase of the far-field pattern was adjusted to account for the probe distance during measurement. The probe pattern is convolved with the near-field distribution as it moves across the face. Because we have a planar surface, the near-field distribution includes the Huygens source pattern of an aperture. We use the inverse fast Fourier transform (FFT^{-1}) to find the far-field pattern where the result is the product of the aperture pattern and the probe antenna. When inverse transformed from the far-field, after the pattern of the probe and the Huygens source are removed, back to the near-field, the actual distribution across the array elements is found. As pointed out in Section 12-9, we can repeat this at many planes and find the distribution along

the surface of a paraboloidal reflector or other non-planar surface. Generally, planar near-field measurements are restricted to antennas with high gain and narrow beamwidths.

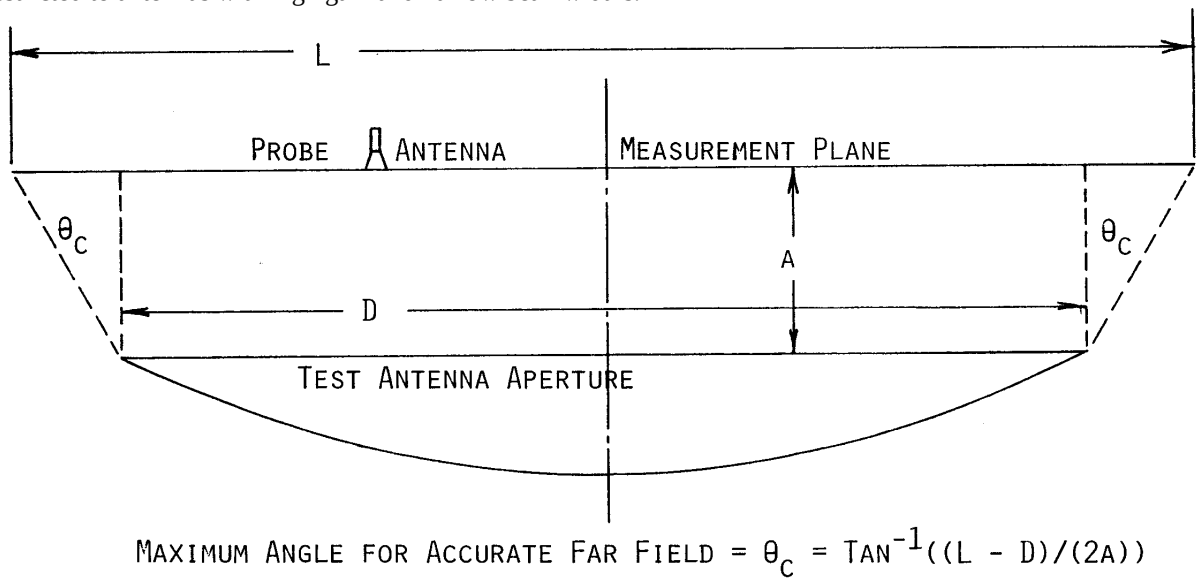

Figure 13-25 Planar near-field measurement

Figure 13-25 illustrates the measurement configuration of a planar near-field. We locate the probe a distance a at least 3λ above the reflector rim or planar array surface to prevent collection of excessive near fields of the elements. To accurately measure the pattern to an angle θ_c off broadside, we extend the measurement line L.

$$\theta_c = \tan^{-1}\left[\frac{L-D}{2a}\right] \quad \text{or} \quad L = D + 2a\tan\theta_c \tag{13-23}$$

In Section 13-8 we applied the FFT to time (distance) and frequency measurements. For apertures we use the Fourier transform between distribution and pattern measured in sin θ space or k_x and k_y space (Section 2-2, Huygens source approximation). We calculate the range of k_x-space from the aperture sampling spacing d [Eq. (12-37)].

$$\sin\theta_{\max} = \pm\frac{\lambda}{2d} \tag{12-37}$$

Equation (12-37) says that the minimum collection spacing is λ/2 because sampling at a closer spacing gives $\theta_{\max}$ in invisible space.

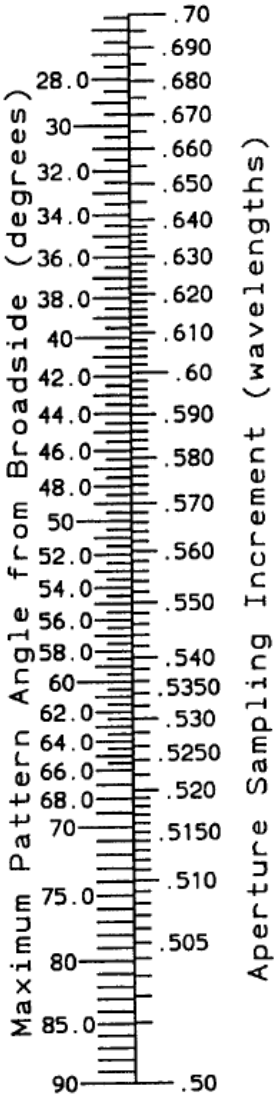
Maximum Pattern Angle from Broadside (degrees)
28.0
30
32.0
34.0
36.0
38.0
40
42.0
44.0
46.0
48.0
50
52.0
54.0
56.0
58.0
60
62.0
64.0
66.0
68.0
70
75.0
80
85.0
90
.70
.690
.680
.670
.660
.650
.640
.630
.620
.610
.60
.590
.580
.570
.560
.550
.540
.5350
.530
.5250
.520
.5150
.510
.505
.50
Aperture Sampling Increment (wavelengths)

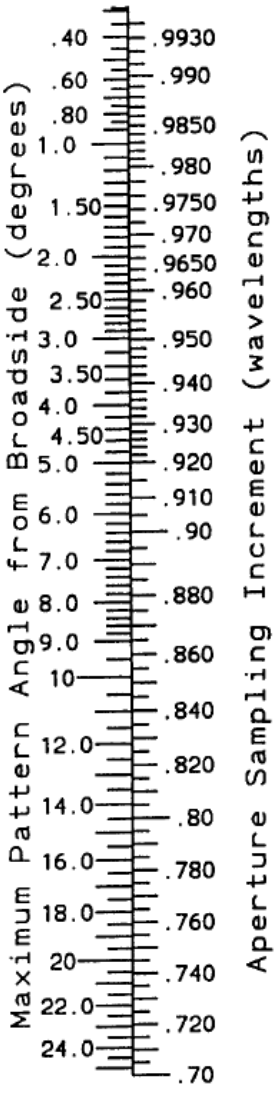
Maximum Pattern Angle from Broadside (degrees)
.40
.60
.80
1.0
1.50
2.0
2.50
3.0
3.50
4.0
4.50
5.0
6.0
7.0
8.0
9.0
10
12.0
14.0
16.0
18.0
20
22.0
24.0
.9930
.990
.9850
.980
.9750
.970
.9650
.960
.950
.940
.930
.920
.910
.90
.880
.860
.840
.820
.80
.780
.760
.740
.720
.70
Aperture Sampling Increment (wavelengths)

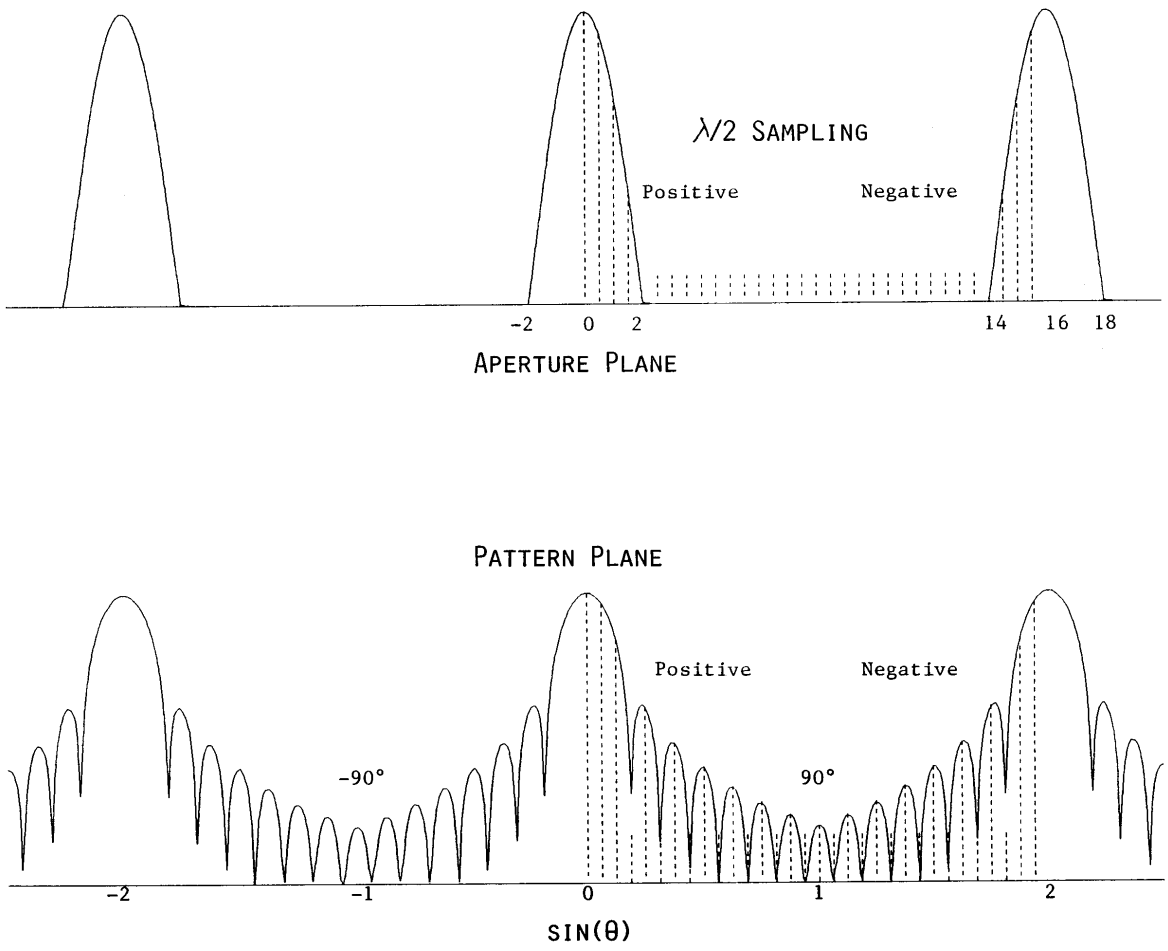

Figure 13-26 Near field sampling at λ/2 increments and corresponding FFT transformed pattern.

Figure 13-26 illustrates the steps in a near-field sampling when the FFT is applied using only 32 sampling points. The discrete Fourier transform (DFT) must be arranged from zero to maximum positive point and then most negative to least negative point. The DFT, calculated using the FFT, is a periodic function similar to the Fourier series used with an array. The FFT has the same number of points as the near-field and does not produce the smooth pattern as shown in Figure 13-26(*b*) but only values at the dotted vertical lines. We calculate the spacing in k_x from the total span of the near-field sampling. Since the FFT requires 2^N samples,

$$\Delta k_x = \frac{\lambda}{2^N 2d} \tag{13-38}$$

We decrease the pattern spacing by zero padding the near-field sampling before the FFT. We can see that the space between the two portions of the repeating aperture distributions already has many points with low values. We can add more points and stretch the distance between the positive and negative apertures and reduce the sin θ increments. Of course, this increases the FFT calculation time and produces many unnecessary wide angle pattern points. We will apply a technique to resolve the pattern that uses the FFT to interpolate points without increasing the size of the FFT but eliminates wide angles.

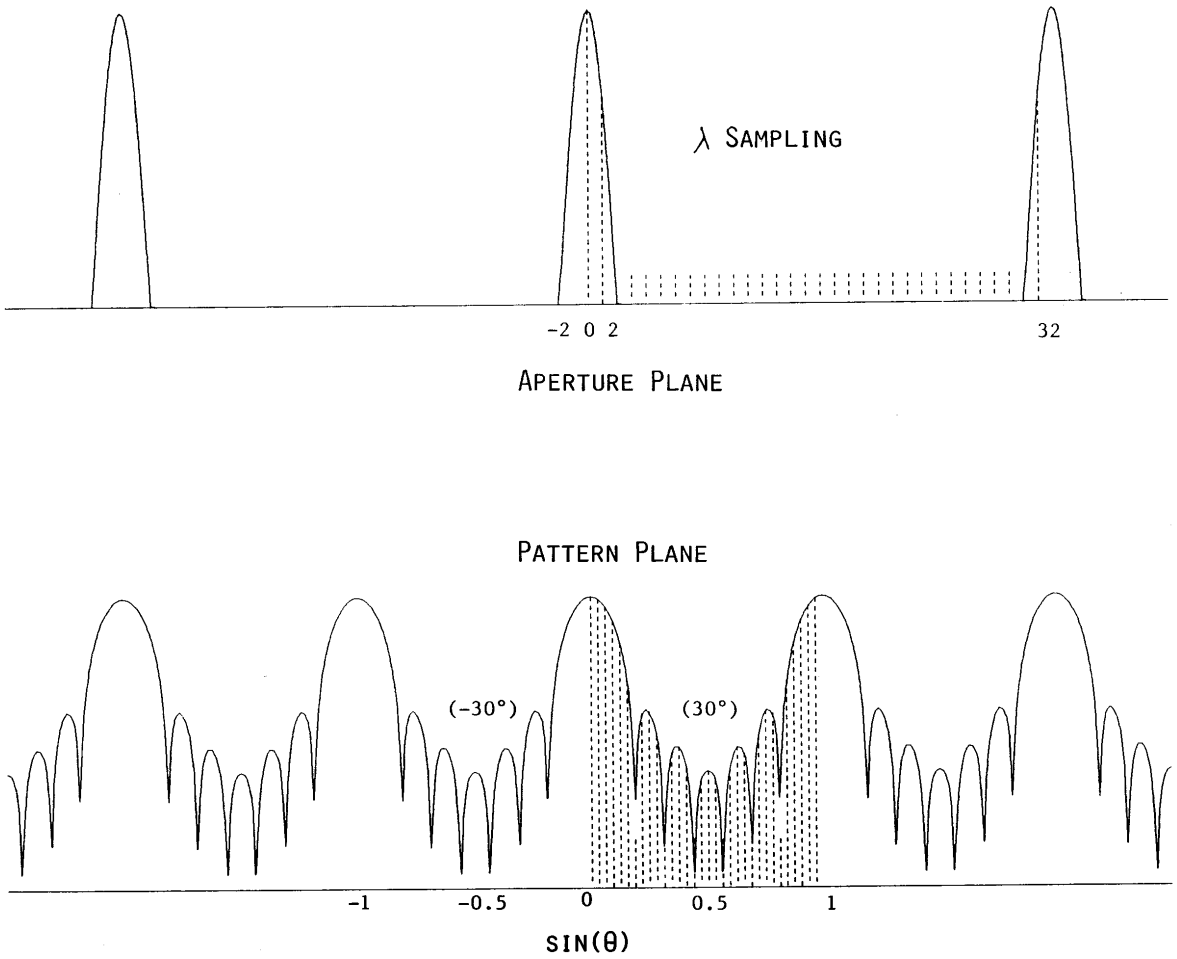

Figure 13-27 Near field sampling at λ increments and corresponding FFT transformed pattern.

Figure 13-27 illustrates a measurement using a λ near-field spacing and the corresponding pattern that now repeats at 30º. This measurement has 32 points in the transform and has greater resolution in the far-field pattern. Similar to Figure 13-26, the smooth pattern curve was found by interpolation between actual transformed points. Figure 13-28 shows what happens when we sample at λ/4 near-field spacing. The FFT produces pattern points in invisible space, that is, beyond 90º. We fail to gain pattern information although we have better knowledge of the aperture distribution. This illustrates that we could zero pad the far-field k_x-space in Figure 13-26 and transform back to the near-field and interpolate points in the aperture plane. This operation increases the size of the transform that requires a longer calculation time and larger storage.

13-10.1 Sampling Errors in Near-field Measurements

Planar near-field is a windowing function on the aperture whose filtering action produces Gibbs ripple in the pattern calculated from the transform. Figure 13-29 shows the DFT of a 51 element array sampled in the near field and then transformed to the far field (red). The blue curve shows the aperture pattern. The sampling is equivalent to DFT in the use of the Fourier series on the array. All distributions with a stepped edge transition exhibit the same error near the crossover point in *k*-space and the sampled pattern is higher than the aperture pattern. When the aperture distribution approaches the edge in a linear function with a zero on the edge, the sampled pattern is less than the aperture pattern. These errors depend only on the edge condition and not the general aperture distribution. The uniform distribution has the same errors near the crossover as the Taylor distribution. This characteristic limits the range of valid patterns in a near field measurement dependent on the aperture edge condition.

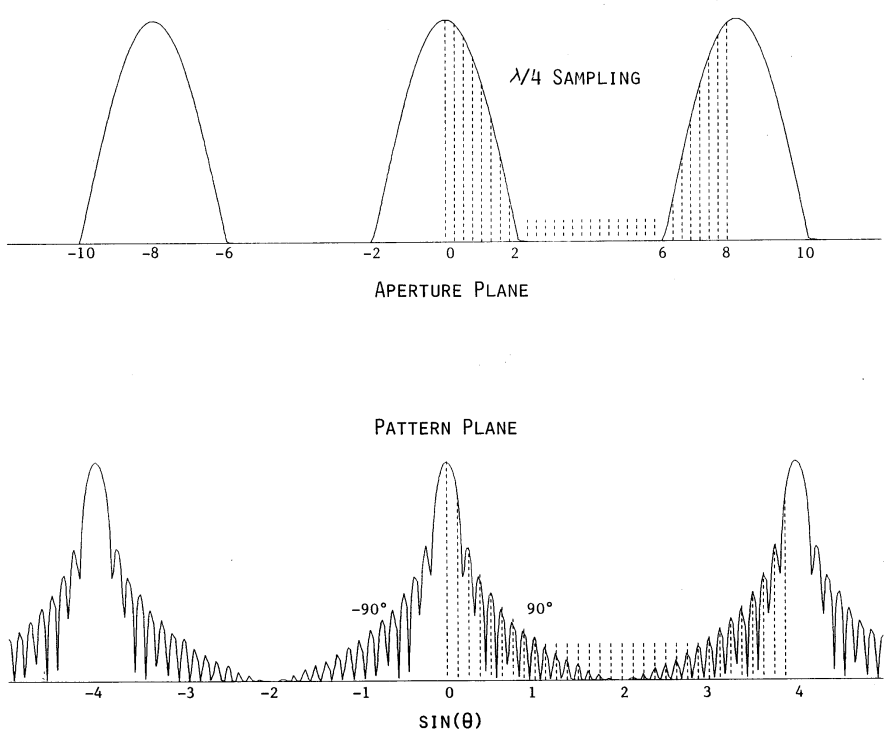

Figure 13-28 Near field sampling at λ/4 increments and corresponding FFT transformed pattern.

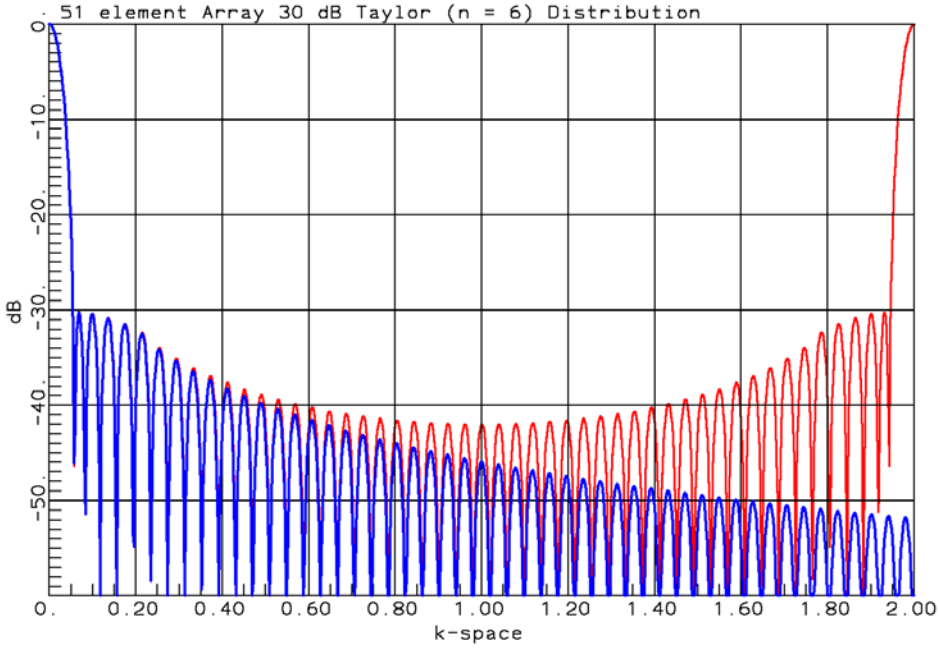

Figure 13-29 Sampling pattern error due to DFT on 51 element array (*a*) aperture (blue), (*b*) array (red)

Figure 13-30 gives the sampling error scales for the edge conditions: (*a*) uniform step, (*b*) linear slope, and (*c*) quadratic slope (derivative is zero at edge), as a function of the *k*-space value at crossover. We use these to determine the measurement error off broadside in a planar near-field measurement.

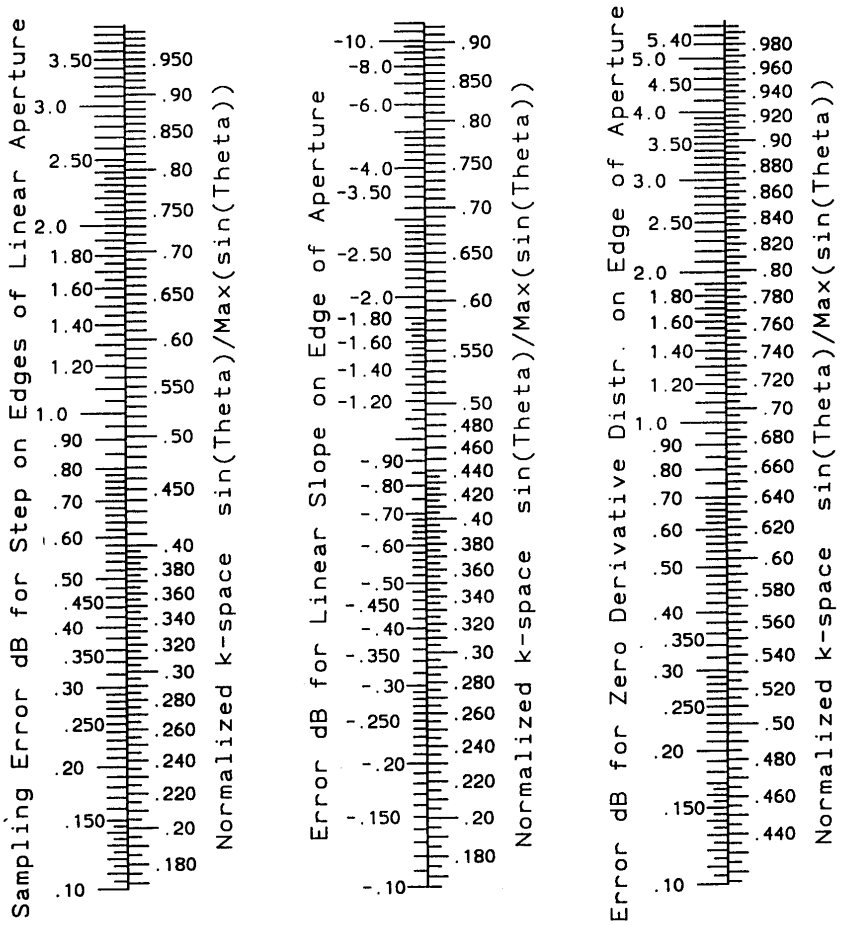

Figure 13-30 Sampling error approaching crossover point in *k*-space pattern dependent on aperture edge condition

Newell [1] calls for increased aperture sampling to limit planar near-field sampling errors.

$$\theta_{\max} = \sin^{-1}\left(\frac{\lambda}{d} - 1\right) \text{ or } d = \frac{\lambda}{1+\sin\theta_{\max}} \qquad (13\text{-}39)$$

Example Compute the sampling spacing for crossover at 30º and evaluate errors at maximum angle. Normal sampling spacing is λ from Eq. (12-37). When we apply the right equation of Eq. (13-39), we calculate $d = \lambda/(1 + \sin(30º)) = 2\lambda/3$. This new spacing increases the *k*-space crossover point [Eq. (12-37)] k_{max} = ¾ that corresponds to a crossover angle of 48.59º. We compute the normalized *k*-space $k/k_{max} = 2/3$ and read the errors from the scales in Figure 13-30. For an aperture with step on the edge the maximum error is 1.65 dB, that is, the level measured would be higher than actual. The measurement would be low by 2.7 dB for an aperture with a linear slope to zero on the edge.

[1] A. C. Newell, Error analysis techniques for planar near-field measurements, *IEEE Transactions on Antennas and Propagation*, vol. AP-36, no. 6, June 1988, pp. 754-768.

Because we locate the probe at least 3λ above the aperture or array and the measurement includes convolution with the probe pattern, the window edge has a greater fall-off. This tapers the window caused by sampling and reduces error to sampling spacing with its edge step.

13-10.2 FFT Resolve or Interpolating of Planar Near-field

We can zero-pad the FFT sampling to increase the number of pattern points calculated from a planar near-field. This increases the size of the FFT and greatly increases storage requirements when computing a 2-dimensional FFT. The

2-dimensional FFT computes the transform along all rows and then along all columns to find the planar *k*-space pattern. These steps produce many pattern points of little interest and greatly increase the computation burden. We can resolve to more pattern points near broadside by removing points in the FFT pattern and perform two additional shorter FFT operations to find these pattern points.

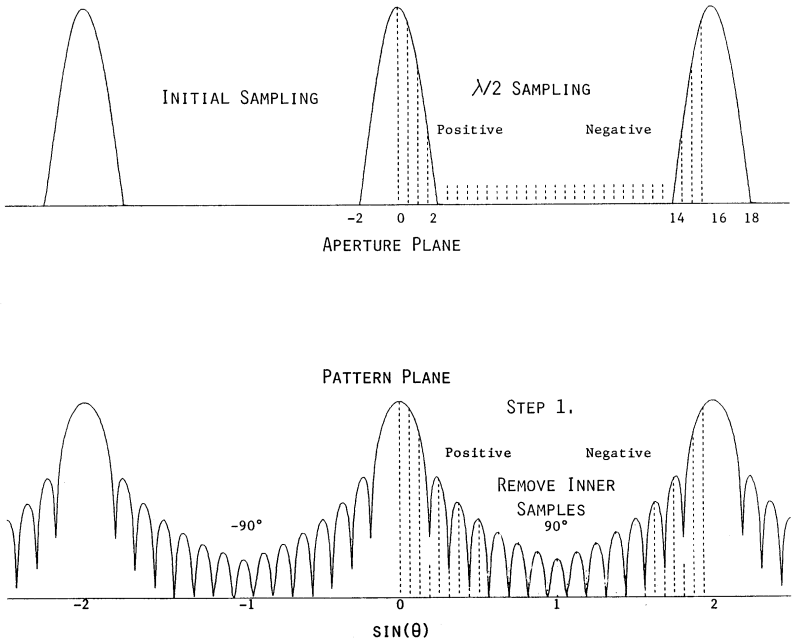

Figure 13-31 Step 1 in FFT resolve of linear aperture pattern

Figure 13-31 illustrates the first step of the pattern resolve. We perform the FFT to calculate the pattern from the aperture sampling and remove inner samples centered at 90º. To double the number of points, we remove half the points. We increase the number of pattern points by four by removing ¾ of the points.

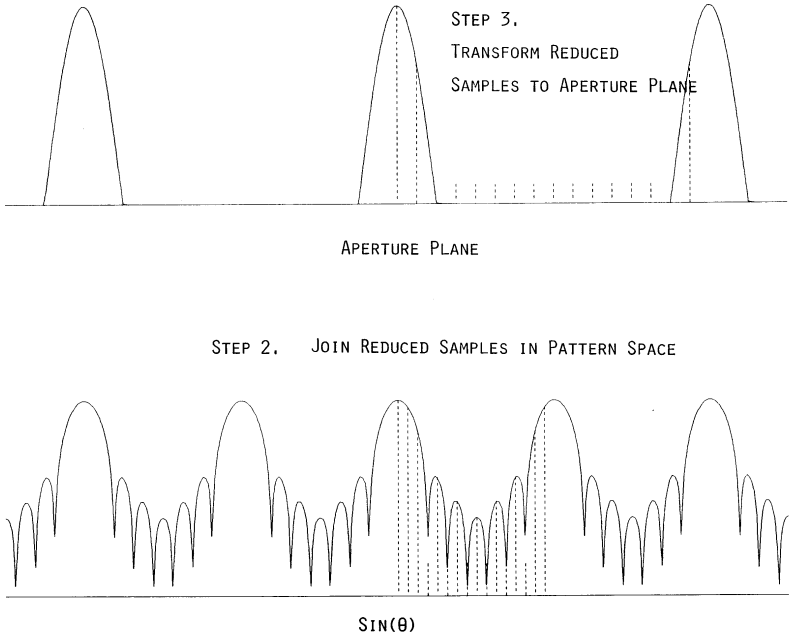

Figure 13-32 Steps 2 and 3 in FFT resolve of linear aperture pattern

Figure 13-32 shows the second step of the FFT resolve. The two sections with their center elements removed are pushed together and joined to generate a reduced length FFT sampling. When we transform this to the aperture plane (Step 3), the sampling spacing is increased.

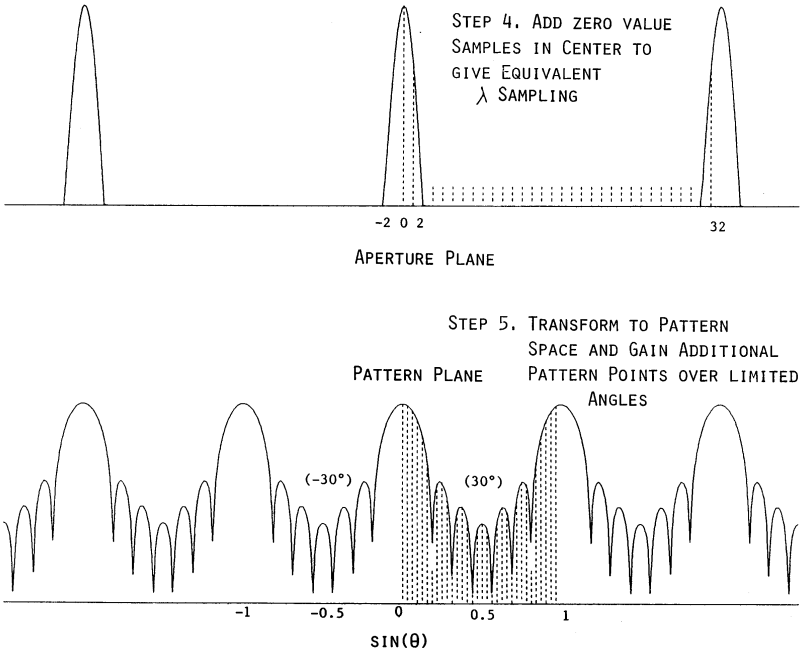

Figure 13-33 Steps 4 and 5 in FFT resolve of linear aperture pattern

In steps 4 and 5 of the FFT resolve (Figure 13-33), the new aperture plane is zero padded to increase the number of points to the original FFT sampling number. Step 5 uses the FFT to find additional pattern points near broadside. The initial sampling allows calculation of the pattern over the entire desired region determined by the near-field sample spacing. The FFT resolve interpolates the pattern to increase the number of points centered on pattern directions of interest. The FFT algorithm has interpolated the pattern without requiring a large storage and associated increased computation cost.

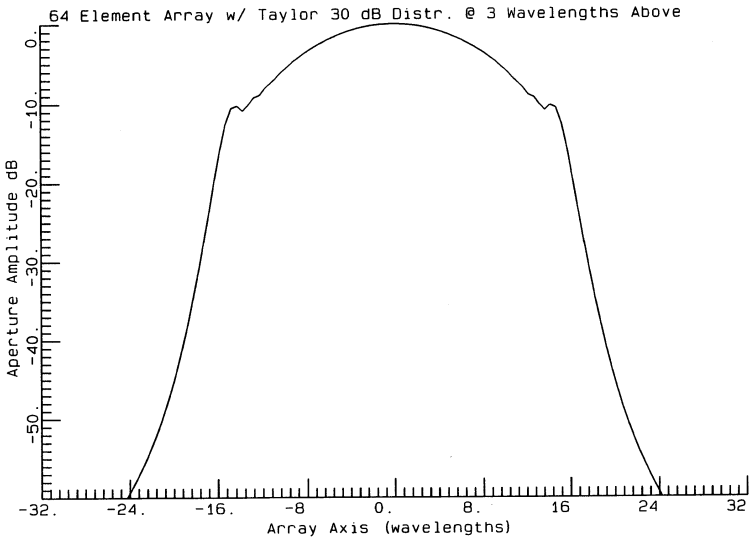

Figure 13-34 Aperture plane sampling of 64 element array with a probe 3λ above array whose amplitudes were found by sampling 30 dB Taylor distribution.

The advantages of the FFT resolve can be shown in an example. Figure 13-34 gives the amplitude distribution found by sampling at 64 element array with λ/2 spacing with a probe located 3λ above its elements. We reduce the coupling between the near-fields of the elements by spacing the probe away from the elements. The near-fields attenuate as $1/R^2$ and $1/R^3$ from the elements to the probe leaving only the far-field terms significant. The Taylor distribution has a step function at its edge. Figure 13-34 shows a tapered edge distribution. The movement of the probe produces a convolution between the probe and the array elements that causes this distribution spread. We transform the aperture distribution to the far-field using the FFT and obtain Figure 13-35. This plot has poor resolution near boresight and does not show the sidelobe details. Figure 13-36 is the fourfold FFT resolve of the pattern plot (Figure 13-35) and now clearly shows the inner sidelobe detail.

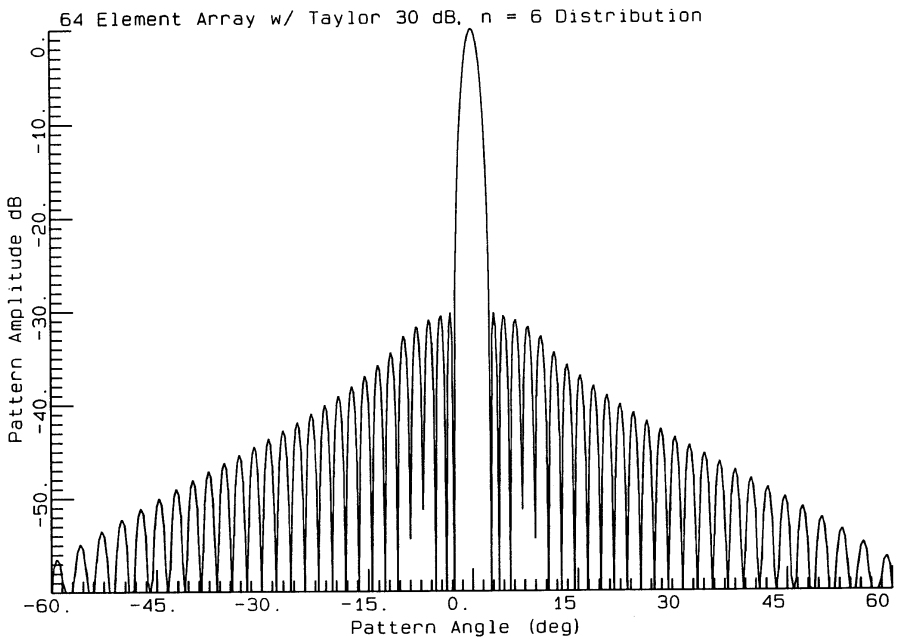

Figure 13-35 Far-field pattern response obtained by the FFT of the aperture distribution of Figure 13-34.

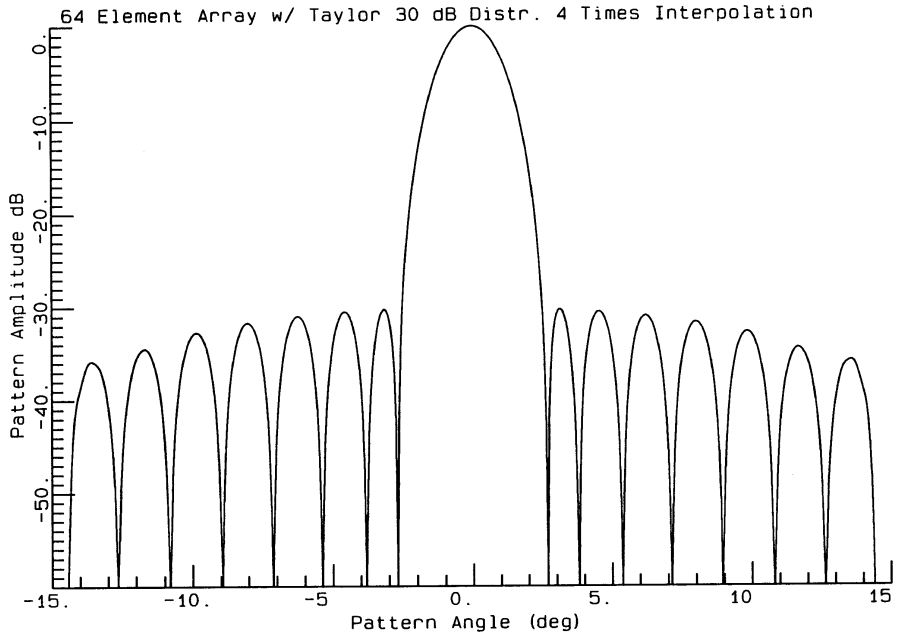

Figure 13-36 Fourfold FFT resolve of the pattern plot of Figure 13-35

13-11 Spherical Near-field range

One this range we measure the pattern over a portion of a sphere and expand the measurements in a series of spherical modes. We use this expansion to compute the pattern at any other radius including the far-field. By limiting the number of terms in the expansion, we attenuate antenna range reflections and eliminate multipath. A general spherical measurement on a model tower can be reduced to a series of spherical modes and used into interpolate the pattern and eliminate multipath as well as account for near-field characteristics of the feed for general scattering problems, for example, a paraboloidal reflector. Besides using a model tower positioner to collect data on a sphere where the source antenna (or probe) is moved close to the positioner, an arch positioner (Figure 13-37) is used for spherical near-field measurements. The arch needs to be covered with absorber to reduce the multipath at nearly the same radius as the probe. These reflections cannot be removed by limiting the number of modes.

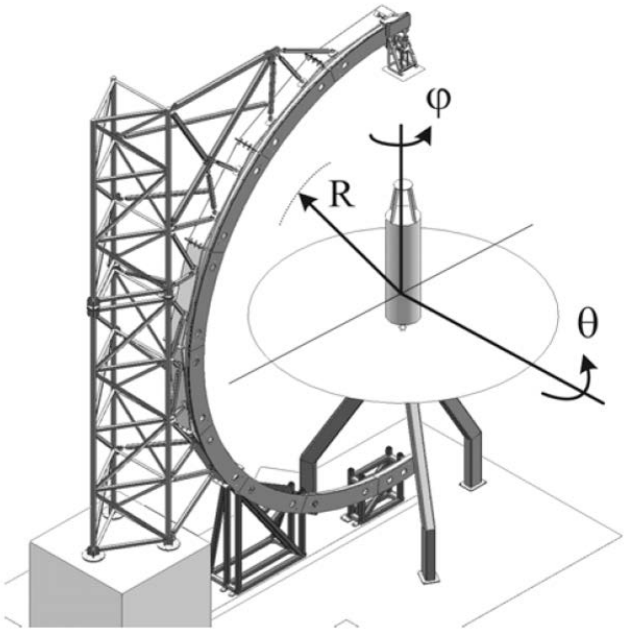

Figure 13-37 Arch positioner combined with azimuth table for spherical near-field measurements

Given the radius of the measurement sphere r_0, the number of modes in the expansion N is given by [1]

$$N = \text{int}[kr_0] + 10 \quad \text{where } k = \frac{2\pi}{\lambda} \tag{13-40}$$

Positioning errors have significant effect on the mode coefficients and must be controlled better than typical model tower.

[1] J. E. Hansen, ed., *Spherical Near-field Antenna Measurements*, Peter Peregrinus, London, 1988, p. 21.

Outdoor Spherical Arch Positioner

13.12 Measuring Antenna using RCS

Small broad-beam antennas present a particular difficult measurement problem. It is difficult to mount them on a model tower positioner and not have the polarization positioner add a ground plane. Some of these antennas lack a proper balun and currents on the feed cable to the receiver radiate. We reduce the cable radiation by covering the cable with ferrite beads that have limited effectiveness. Another solution is to receive the signal with a battery operated receiver and re-radiate the received signal at a different frequency or at IR. Without a reference signal, we cannot measure phase.

If a radar cross section (RCS) range is available, we can measure the pattern from two RCS measurements. We divide the RCS into two parts: (1) antenna mode where the signal power appears at the input that can be absorbed or reflected to be re-radiated and (2) the structure mode where the antenna reflects signals independent of the input load. By using two measurements with different input terminations, we can subtract the structure mode RCS and convert the remaining term to antenna gain. Antennas such as dipoles have the same current distribution whether terminated with a matched load or a short circuit. If we place an open circuit termination on a dipole, if becomes two half length shorted dipole antennas, which has a different current distribution. Slot antennas have just the opposite current distributions and we need to use a matched load and open circuit termination.

RCS ranges have unique measurement problems. When we transmit a signal into an anechoic chamber, the return signal is large compared to the object reflected signal. We use hardware or software gate centered on the object to eliminate these reflections. We start with a background measurement that we will subtract from the measured object reflections that enables measurement at a series of frequencies to allow a software gate. In a earlier method of measuring RCS, a portion of the transmitted CW signal was added to the receive signal and its amplitude and phase was adjusted to null out the received background signal. This tedious process was eliminated by signal processing

on digitized signals. The stability of the generator was eliminated by using synthesized sources, but the stability of the chamber remains a problem. As the external and internal temperature of the walls change, the walls will move slightly and raise the background reflection remaining after subtraction of measurements. One solution is place the chamber inside a building so that the double wall construction reduces the effects of outside weather. Nevertheless, a background can be held only for a short time.

We mount the antenna on a foam- or shaped-column for measurement. Before the measurement, we measure the empty chamber and column to find the background reflection. To calibrate the returned signals, we mount a sphere on the column whose RCS can be calculated for a given frequency. We mount the object on the column and calculate its RCS from a third measurement.

$$\text{RCS (voltage)} = \frac{\text{Object - Background}}{\text{Calibration Sphere - Background}} \text{RCS (sphere)} \qquad (13\text{-}41)$$

We measure the antenna twice: (1) matched termination on antenna terminals, (2) short circuited termination on the antenna. We calculate the pattern gain through subtraction of the structure mode RCS.

$$Gain(voltage) = \frac{\sqrt{4\pi}}{\lambda}\left[\text{RCS (loaded) - RCS(shorted)}\right] \qquad (13\text{-}42)$$

13-14 G/T Measurement

G/T depends on antenna pointing, frequency, and the receiver noise temperature (Section 1-10). We measure G/T using a Y-factor measurement where we compare the noise power out of the receiver when the antenna is pointed toward a hot source to when it is pointed at a cold source. Because we merely add the sky temperature to cascaded antenna losses noise temperature plus receiver noise temperature, we easily separate the system noise temperature. Y-factor is the measured ratio of noise power, $Y = P_{\text{hot}}/P_{\text{cold}}$. If the hot measurement would saturate the receiver, we place a precision attenuator after the LNA so varying it has little effect on the receiver noise temperature and measure Y by subtracting attenuator settings. A spectrum analyzer and other receivers do not measure power accurately [1] so the precision attenuator is used to measure the difference between the hot and cold measurements. The system noise temperature is computed from the noise temperatures.

$$T_e = \frac{T_{hot} - YT_{cold}}{Y - 1} \qquad (13\text{-}43)$$

The measurements can be performed outdoors with the antenna pointed toward the sky for the cold measurement where it is either performed at night or the antenna main beam and major sidelobes avoid sun. We use Figure 1-8 to determine the sky temperature. We cover the antenna with an absorber lined box for the hot measurement. For a wide beamwidth antenna we cover the whole antenna and the ground plane, whereas we cover only the feed for a reflector antenna. The hot temperature is the physical temperature of the absorber. Indoor measurements have been tried using absorber soaked in liquid nitrogen for the cold measurement, but this measurement is stable for only 10 to 20 seconds. We point the antenna into the chamber for the hot measurement. Of course, the gain is measured separately.

We can use the solar flux to measure narrow beamwidth antennas to measure G/T directly. We point the antenna away from the sun for the cold measurement and point the main beam at the sun for the hot measurement. It may be necessary to add the precision attenuator after the LNA to prevent receiver saturation when pointing at the sun. With $Y = P_{\text{sun}}/P_{\text{sky}}$, we calculate the system G/T.

$$\text{G/T} = \frac{(Y-1)8\pi kL}{F\lambda^2} \tag{13-44}$$

k = 1.38 x 10^{-23} joule/K (Boltzman's constant)
F – solar flux @ f_0 w/m^2/Hz
L – beamwidth correction factor = 1 for beamwidth larger than 2º

$$L = 1 + 0.38\left(\frac{w_s}{w_a}\right)^2$$

w_s – diameter of the radio sun in degrees @ f_0: 0.5º for f_0 > 3000 MHz, 0.6º for 1420 MHz, and 0.7º for 400 MHz
w_a – antenna 3-dB beamwidth

The solar flux, F, is available online @ 245, 410, 610, 1415, 2695, 4995, 8800, and 15400 MHz. The values reported must be multiplied by 10^{-22}. We interpolate F for frequencies between these.

An artificial radio star can be used to measure G/T inside a chamber [2]. A noise generator is connected to an amplifier and a transmit antenna inside the chamber. The cold measurement is the absorber. A standard gain horn is attached to an amplifier with a measured noise temperature to serve as a G/T standard. We determine the G/T of the unknown antenna and receiver by performing Y-factor measurements on both antennas.

$$G_2/T_2 = \frac{(G_1/T_1)(Y_2-1)}{Y_1-1} \tag{13-45}$$

We can extend Eq. (13-45) to any Y-factor measurement of G/T when we have established a G/T standard.

Let us extend our discussion to relate the chamber measurements to the final system. We generate the artificial radio star by connecting an excess noise source to the transmit antenna. The amount of noise which reaches our antenna under test is found from path loss considerations. In normal antenna measurements we eliminate the need to know exact path loss by using a gain standard. The antenna and its network, which could include a beamformer and amplifiers, are connected to a receiver. We divide the receive system into three components: a lossless antenna (directivity), the combination of antenna losses and feed network, and the measurement receiver. To represent the excess noise present at the antenna, we use a hot source temperature T_{HS} which when multiplied by the directivity gives us the additional noise at the antenna terminals. The antenna receives the noise due to the chamber walls T_c whether the excess noise source is on or off. Our lossless antenna has a gain G_a and is connected to a network with gain G_n and noise temperature T_n where the noise contributions of the antenna (ohmic losses and mismatch) are included in the network. Let us refer the noise temperature to the input of the receiver with noise temperature T_{mr} by multiplying the noise power by the various stages.

$$P_{Cold} = kB\left(T_cG_n + T_nG_n + T_{mr}\right)$$

$$P_{Hot} = kB\left(T_{HS}G_aG_n + T_cG_n + T_nG_n + T_{mr}\right)$$

The noise received by the antenna from the chamber walls is independent of the antenna gain since it is the integral of gain angular distribution times a constant temperature T_c. The integral of the gain function over all space is one.

We use the receiver to measure the ratio of the two powers Y.

$$Y = \frac{P_{Hot}}{P_{Cold}} = \frac{kB\left(T_{HS}G_aG_n + T_cG_n + T_nG_n + T_{mr}\right)}{kB\left(T_cG_n + T_nG_n + T_{mr}\right)}$$

$$Y = \frac{T_{HS}G_a + T_c + T_n + T_{mr}/G_n}{T_c + T_n + T_{mr}/G_n}$$

We see from the equation above that when we measure a device with significant gain, we can ignore the noise temperature of the receiver.

$$Y = \frac{T_{Hot} + T_n + T_{mr}/G_n}{T_{Cold} + T_n + T_{mr}/G_n}$$

$$T_n = \frac{T_{Hot} - YT_{Cold}}{Y-1} - \frac{T_{mr}}{G_n} \qquad (13\text{-}46)$$

Equation (13-46) is the normal Y factor measurement equation for a device when the noise temperature of the receiver is included [1].

When measuring the antenna, we compute the network and antenna losses combination noise temperature from the following equation.

$$T_n = \frac{T_{HS}G_a + T_c(1-Y)}{(Y-1)} - \frac{T_{mr}}{G_n} \qquad (13\text{-}47)$$

We measure with a gain standard to determine T_{HS}. Given the directivity of the gain standard D_s, associated losses due to mismatch and material losses $L_s = 1/G_n \approx 1$, and equivalent noise temperature due to theses losses when referred to the directivity terminals $T_s \approx 0$, we perform a Y-factor measurement using the receiver to obtain the value Y_s.

$$T_{HS} = \frac{\left(Y_s - 1\right)\left(T_c + T_s + T_{mr}L_s\right)}{D_s} \qquad (13\text{-}48)$$

Both equations (13-47) and (13-48) contain the noise temperature of the receiver. We use the excess noise source to measure the noise temperature of the receiver system which often includes an amplifier located near the antenna and a long cable that delivers the signals to a spectrum analyzer. The excess noise source (diode) delivers a temperature T_0 when off and T_0 (ENR+1) across a wide frequency range when on. The bandwidth of the spectrum analyzer narrows the frequency bandwidth for measurement.

$$T_{mr} = T_0\left[\frac{ENR}{\left(Y_r - 1\right)} - 1\right] \qquad (13\text{-}49)$$

We combine equations (13-47), (13-48), and (13-49) to compute the noise temperature of the feed network and antenna combination referred to the directivity point of the antenna. We obtain the G/T for the measurement in the chamber by the ratio of the product of gains divided by the noise temperature referred to the input to the measurement receiver.

$$G/T = \frac{G_aG_n}{(T_c + T_n)G_n + T_{mr}} = \frac{G_a}{\dfrac{T_{HS}G_a + T_c(1-Y)}{Y-1} + T_c} \qquad (13\text{-}50)$$

Equation (13-50) does not include the noise temperature of the measurement system, but gives G/T for the antenna attached to the measurement receiver.

Given the Y factor measured in the chamber with the associated T_{HS} and measurement receiver noise temperature T_{mr}, we compute G/T during operation from the antenna sky temperature T_a, and the operating receiver noise temperature T_r.

$$\frac{G_{sys}}{T_{sys}} = \frac{(Y-1)}{T_{HS} + (Y-1)\left(\frac{T_a - T_c}{G_a} + \frac{T_r - T_{mr}}{G_a G_n}\right)} \tag{13-51}$$

$$\frac{G_{sys}}{T_{sys}} = \frac{(T_c + T_n)G_n + T_{mr}}{(T_a + T_n)G_n + T_r}(G/T)_{chamber}\, G_{scan} \tag{13-52}$$

Equation (13-52) shows the effects of the actual receiver and antenna temperature. G_{scan} is the gain reduction due to scanning the beam. If the network gain changes with scan, then the denominator term needs to be changed while the numerator term is the same as the measurement.

[1] Peter Vizmuller, *RF Design Guide, Systems, Circuits and Equations*, Artech, 1995, pp. 192-196.
[2] Dean Paschen, Peter Moosbrugger, and Timothy Meenach, Active and Adaptive Antenna Testing, AMTA

13-15 Error Measuring LHC Antenna with Cross Linear Source

The vector response of the antenna under test is given by

$$\begin{aligned}\mathbf{E_a} &= E_L\left(\mathbf{a}_L + \hat{\rho}_{\mathbf{C}}\mathbf{a}_R\right) = \frac{E_L}{\sqrt{2}}\left[\left(\mathbf{a_x} + j\mathbf{a_y}\right) + \hat{\rho}_{\mathbf{C}}\left(\mathbf{a_x} - j\mathbf{a_y}\right)\right] \\ &= \frac{E_L}{\sqrt{2}}\left[\mathbf{a_x}\left(1+\hat{\rho}_{\mathbf{C}}\right) + j\mathbf{a_y}\left(1-\hat{\rho}_{\mathbf{C}}\right)\right]\end{aligned} \tag{1}$$

The unit vector of the linear measurement antenna along *x*-axis is

$$\frac{\mathbf{a_x} + \hat{\rho}_{\mathbf{Lx}}\mathbf{a_y}}{\sqrt{1+\left|\hat{\rho}_{\mathbf{Lx}}\right|^2}} \tag{2}$$

Whereas, the *y*-axis linear measurement antenna has been rotated

$$\frac{-\hat{\rho}_{\mathbf{Ly}}\mathbf{a_x} + \mathbf{a_y}}{\sqrt{1+\left|\hat{\rho}_{\mathbf{Ly}}\right|^2}} \tag{3}$$

The *x*-axis and *y*-axis responses are found by projecting Eqs. (2) and (3) on to Eq. (1)

$$x\text{-axis response}\quad \frac{\frac{E_L}{\sqrt{2}}\left[\left(1+\hat{\rho}_{\mathbf{C}}\right) + j\hat{\rho}_{\mathbf{Lx}}{}^*\left(1-\hat{\rho}_{\mathbf{C}}\right)\right]}{\sqrt{1+\left|\hat{\rho}_{\mathbf{Lx}}\right|^2}} \tag{4}$$

$$y\text{-axis response}\quad \frac{\frac{E_L}{\sqrt{2}}\left[-\hat{\rho}_{\mathbf{Ly}}{}^*\left(1+\hat{\rho}_{\mathbf{C}}\right) + j\left(1-\hat{\rho}_{\mathbf{C}}\right)\right]}{\sqrt{1+\left|\hat{\rho}_{\mathbf{Ly}}\right|^2}} \tag{5}$$

We convert the *x*-axis and *y*-axis responses to circular components by using Eq. (1-39)

$$E_{L,Meas} = \frac{E_L}{2}\left[\frac{\left(1+\hat{\rho}_{\mathbf{C}}\right)+j\hat{\rho}_{\mathbf{Lx}}{}^{*}\left(1-\hat{\rho}_{\mathbf{C}}\right)}{\sqrt{1+\left|\hat{\rho}_{\mathbf{Lx}}\right|^2}}+\frac{j\hat{\rho}_{\mathbf{Ly}}{}^{*}\left(1+\hat{\rho}_{\mathbf{C}}\right)+\left(1-\hat{\rho}_{\mathbf{C}}\right)}{\sqrt{1+\left|\hat{\rho}_{\mathbf{Ly}}\right|^2}}\right] \tag{6}$$

$$E_{R,Meas} = \frac{E_L}{2}\left[\frac{\left(1+\hat{\rho}_{\mathbf{C}}\right)+j\hat{\rho}_{\mathbf{Lx}}{}^{*}\left(1-\hat{\rho}_{\mathbf{C}}\right)}{\sqrt{1+\left|\hat{\rho}_{\mathbf{Lx}}\right|^2}}-\frac{j\hat{\rho}_{\mathbf{Ly}}{}^{*}\left(1+\hat{\rho}_{\mathbf{C}}\right)+\left(1-\hat{\rho}_{\mathbf{C}}\right)}{\sqrt{1+\left|\hat{\rho}_{\mathbf{Ly}}\right|^2}}\right] \tag{7}$$

Consider the relation between the linear and circular polarization ratios of a particular antenna separate from ratios given above for the source and AUT. We find the circular polarization ratio from the ratio of the right-hand and left-hand responses.

$$\hat{\rho}_C = \frac{E_R}{E_L} = \frac{1+j\hat{\rho}_L}{1-j\hat{\rho}_L} \quad \text{and } \hat{\rho}_L = \frac{j\left(1-\hat{\rho}_C\right)}{\left(1+\hat{\rho}_C\right)} \tag{8}$$

When we rotate and antenna about an axis, the magnitude of $\hat{\rho}_C$ remains constant whereas its phase changes. If we rotate the measurement antenna until its polarization ellipse is aligned with the *x*-axis, the tilt angle is zero and so is the phase of $\hat{\rho}_C$ since it is equal to twice the tilt angle. For a linear antenna that is predominately LHC, the magnitude of $\hat{\rho}_C$ is less than one and the phase of the linear polarization ratio is 90º. A linear antenna predominately RHC has a linear polarization phase of -90º.

$$\hat{\rho}_L^{*} = \pm j\left|\hat{\rho}_L^{*}\right| = \pm j\rho_L$$

The upper sign is for a linear antenna predominately RHC and the polarization ratio without the caret is the magnitude. We substitute this into Eqs. (6) and (7).

$$E_{L,Meas} = \frac{E_L}{2}\left[\frac{1+\hat{\rho}_C \mp \rho_{Lx}\left(1-\hat{\rho}_C\right)}{\sqrt{1+\rho_{Lx}{}^2}}+\frac{\mp\rho_{Ly}\left(1+\hat{\rho}_C\right)+\left(1-\hat{\rho}_C\right)}{\sqrt{1+\rho_{Ly}{}^2}}\right] \tag{9}$$

$$E_{R,Meas} = \frac{E_L}{2}\left[\frac{1+\hat{\rho}_C \mp \rho_{Lx}\left(1-\hat{\rho}_C\right)}{\sqrt{1+\rho_{Lx}{}^2}}-\frac{\mp\rho_{Ly}\left(1+\hat{\rho}_C\right)+\left(1-\hat{\rho}_C\right)}{\sqrt{1+\rho_{Ly}{}^2}}\right] \tag{10}$$

If we use the same antenna for both measurements and rotate it to obtain the *y*-axis measurement, the magnitude of the linear polarization ratio is the same. This assumes that the chamber reflections do not change the linear polarization ratio significantly.

$$E_{L,Meas} = \frac{E_L}{2}\left[\frac{1+\hat{\rho}_C+1-\hat{\rho}_C \mp \rho_L\left(1-\hat{\rho}_C+1+\hat{\rho}_C\right)}{\sqrt{1+\rho_L{}^2}}\right] = E_L\frac{1\mp\rho_L}{\sqrt{1+\rho_L{}^2}} \tag{11}$$

$$E_{R,Meas} = \frac{E_L}{2}\left[\frac{1+\hat{\rho}_C-(1-\hat{\rho}_C)\mp\rho_L\left(1-\hat{\rho}_C-(1+\hat{\rho}_C)\right)}{\sqrt{1+\rho_L{}^2}}\right] = E_L\hat{\rho}_C\frac{1\pm\rho_L}{\sqrt{1+\rho_L{}^2}} \tag{12}$$

Equations (11) and (12) give the measurement error due to the source cross-polarization where the upper sign is for a linear antenna predominately RHC and the lower sign for LHC. The error is independent of the axial ratio of the antenna being measured. These are the actual errors and not the range of error.

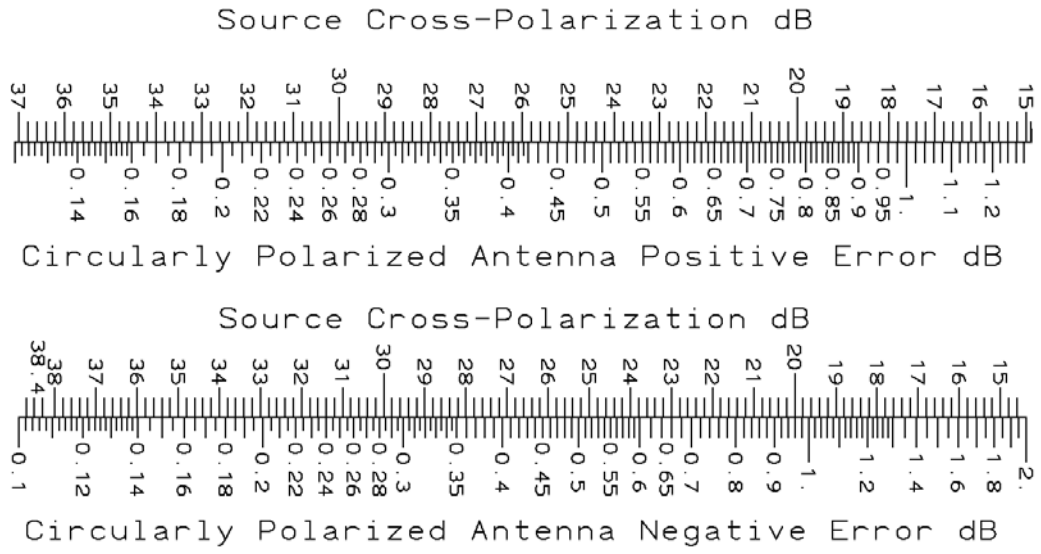

We combine Eqs. (11) and (12) to calculate the measurement error of axial ratio.

$$\text{Axial Ratio} = \frac{|E_L|+|E_R|}{|E_L|-|E_R|} = \frac{1 \mp \rho_L + \rho_C(1 \pm \rho_L)}{1 \mp \rho_L - \rho_C(1 \pm \rho_L)} \tag{13}$$

$$\text{Axial Ratio Error} = \frac{1 \mp \rho_L + \rho_C(1 \pm \rho_L)}{1 \mp \rho_L - \rho_C(1 \pm \rho_L)} \frac{1-\rho_C}{1+\rho_C} \tag{14}$$

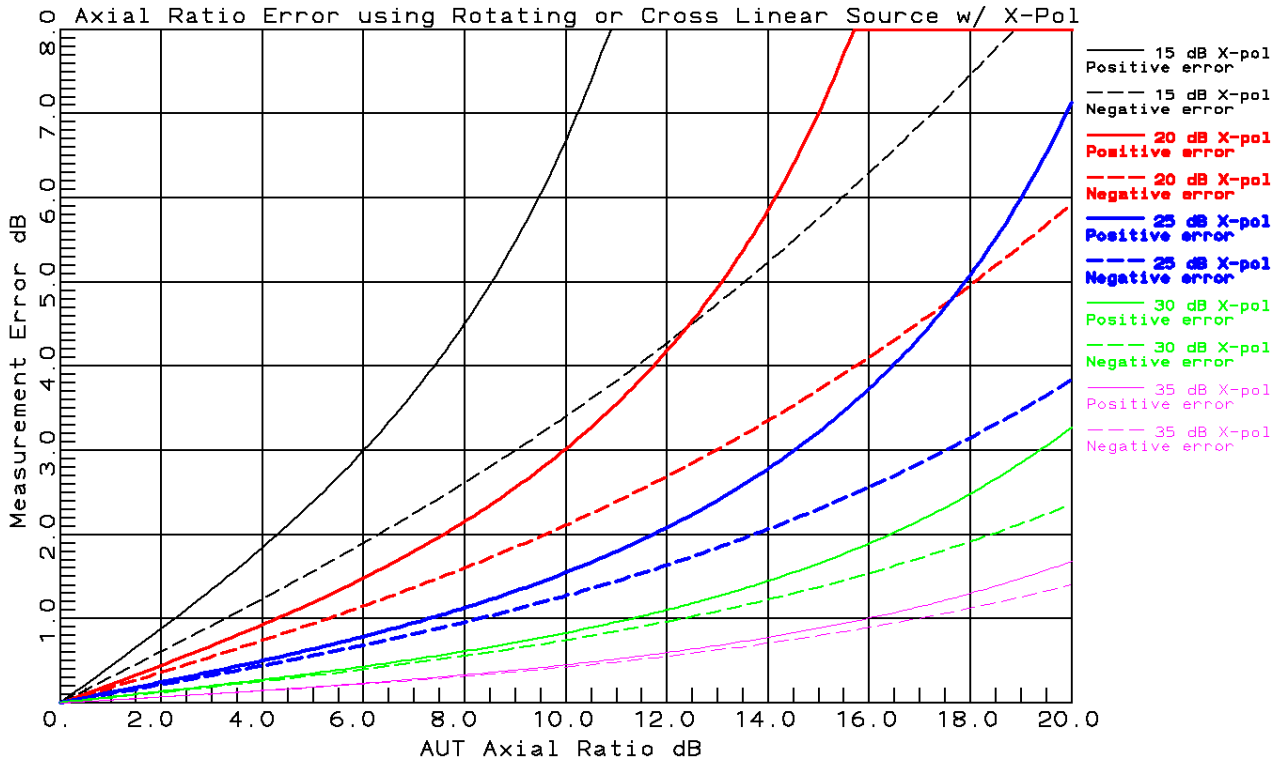

We compute the maximum linear response from the sum of the RHC and LHC components [(Eq. (1-36)].

$$E_{\max} = E_L\left(1+\rho_C\right)/\sqrt{2}$$

$$E_{\max,Meas} = \frac{E_L}{\sqrt{2}}\frac{[1\mp\rho_L+\rho_C\left(1\pm\rho_L\right)]}{\sqrt{1+\rho_L^2}}$$

The measurement error is the ratio including a rearrangement of the terms.

$$\frac{E_{\max,Meas}}{E_{\max}} = \frac{1+\rho_C\mp\rho_L\left(1-\rho_C\right)}{\left(1+\rho_C\right)\sqrt{1+\rho_L^2}} \tag{15}$$

In similar steps we calculate the minimum linear response.

$$E_{\min} = E_L\left(1-\rho_C\right)/\sqrt{2}$$

$$E_{\min,Meas} = \frac{E_L}{\sqrt{2}}\frac{[1\mp\rho_L-\rho_C\left(1\pm\rho_L\right)]}{\sqrt{1+\rho_L^2}}$$

$$\frac{E_{\min,Meas}}{E_{\min}} = \frac{1-\rho_C\mp\rho_L\left(1+\rho_C\right)}{\left(1-\rho_C\right)\sqrt{1+\rho_L^2}} \tag{16}$$

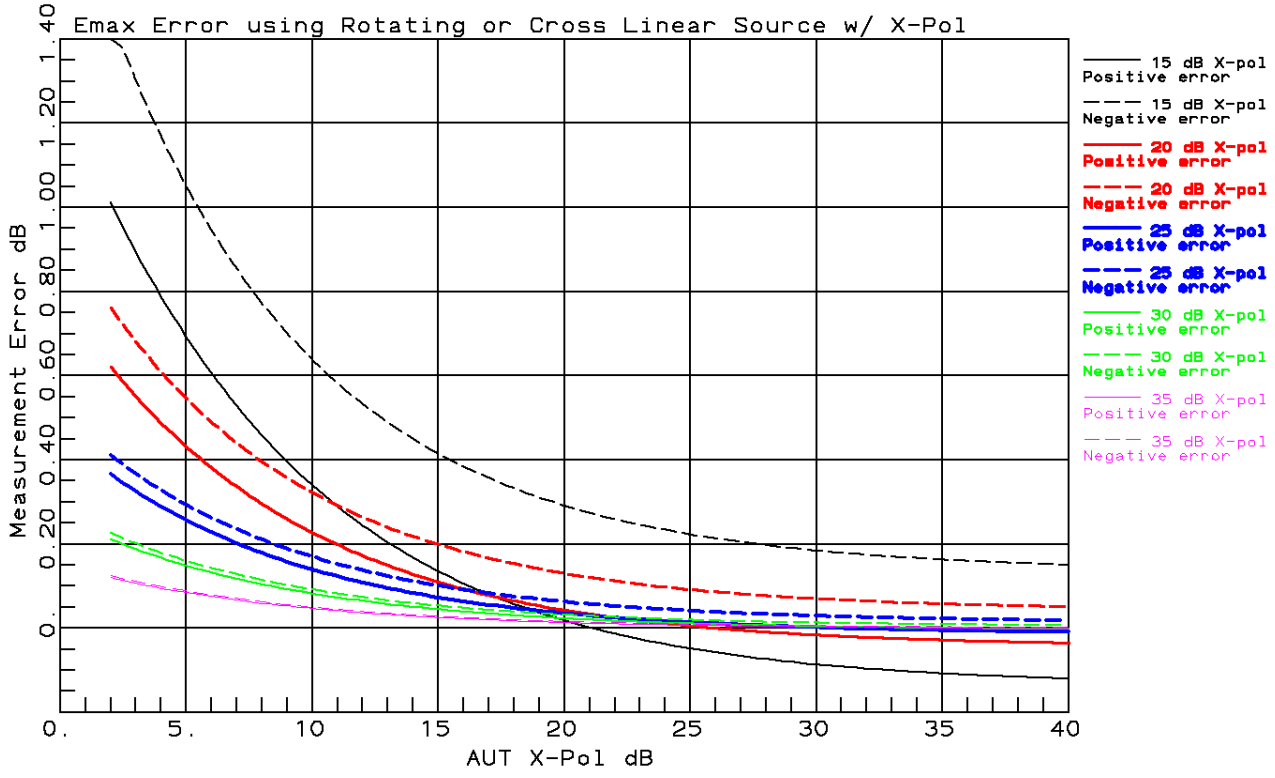

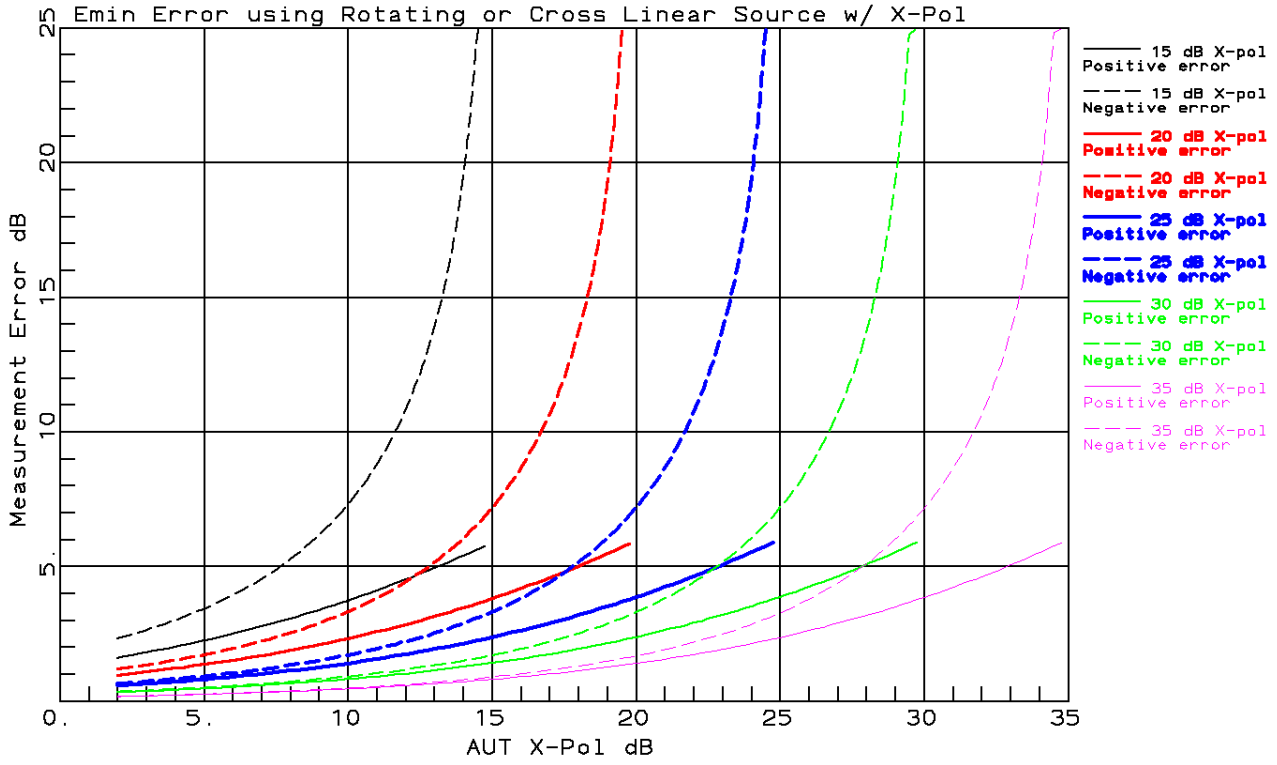

[i] George L. Ragan, ed., *Microwave Transmission Circuits,* McGraw-Hill, 1948, p. 554